

Unveiling competitions between carrier recombination pathways in semiconductors via mechanical damping

Mingyu Xie¹, Ruitian Chen¹, Jiaze Wu¹, Kaiqi Qiu¹, Mingqiang Li¹, Huicong Chen¹, Kai
Huang¹, Yu Zou^{1,a)}

¹Department of Materials Science and Engineering, University of Toronto, Toronto, ON M5S
3E4, Canada

Abstract

The total rate of carrier recombination in semiconductors has conventionally been expressed using an additive model, $r_{total} = \sum r_i$, which rules out the interactions between carrier recombination pathways. Here we challenge this paradigm by demonstrating pathway competitions using our newly developed light-induced mechanical absorption spectroscopy (LIMAS), which allows us to probe genuine recombination dynamics in semiconductors via mechanical damping. We show that the total recombination rate in zinc sulfide (ZnS), a model semiconductor material, follows a multiplicative weighting model, $r_{total} \propto \prod r_i^{w_i}$ with $\sum w_i = 1$. Under both steady-state and switch-on illuminations, the weighting factors w_i for each recombination pathway—direct, trap-assisted, and sublinear—are dictated by the carrier generation mechanism: (i) interband transition favors direct recombination; (ii) single-defect level-mediated generation promotes trap-assisted recombination; (iii) generation involving multiple saturated defect levels gives rise to sublinear recombination. Upon light switch-off, localized state changes drive a dynamic evolution of w_i , altering pathway competitions. These findings reshape our fundamental understanding of carrier dynamics and provide a new strategy to optimize next-generation optoelectronic devices.

Keywords: semiconductors; carriers; mechanical damping; zinc sulfide

^{a)} Author to whom all correspondence should be addressed; Email: mse.zou@utoronto.ca (Y.Z.)

Main

Semiconductors are widely used in LEDs¹, photodetector², and solar cells³, with their optoelectronic properties primarily governed by carrier dynamics, particularly the recombination processes^{4, 5, 6, 7}. Multiple recombination pathways, such as direct, trap-assisted^{8, 9}, sublinear¹⁰, excitonic¹¹, and Auger recombination¹², have been proposed to understand the recombination mechanisms in semiconductors. These specific pathways were characterized using techniques including I - V testing¹³, transient absorption spectroscopy¹⁴, and power-dependent/time-resolved photoluminescence¹⁵ for a wide range of materials, from conventional semiconductors^{12, 16} to hybrid perovskites^{17, 18}. Nevertheless, these techniques typically focus on an individual recombination pathway, thus fitting in a simple additive model ($r_{total} = \sum r_i$, where r_{total} is the total recombination rate and r_i is the rate of each pathway) to predict the overall recombination rate when multiple pathways coexist¹⁹. Although this simplified additive model, also known as the ABC mode¹⁹, has contributed to a fundamental understanding of semiconductors over the past few decades^{6, 20}, there are significant discrepancies between experimental results and theoretical predictions under diverse conditions due to overlooked couplings between the recombination pathways^{21, 22, 23, 24}, impeding the optimization of optoelectronic devices. Recent studies on nanocrystals suggest that recombination pathways can compete rather than act independently. For example, in FAPbBr₃ nanocrystals, excitonic and hot carrier recombination dominate at different wavelengths²⁵, while in InP/CdS and CdSe/Cd_xZn_{1-x}S core-shell quantum dots, the balance among Auger, surface, and hot carrier recombination depends on shell thickness²⁶ and surface passivation²⁷. However, in bulk semiconductors, the direct evidence of such pathway competition remains scarce due to limited proper techniques.

Here we develop light-induced mechanical absorption spectroscopy (LIMAS)—a high-precision mechanical technique that probes genuine recombination dynamics in semiconductors through mechanical damping. Unlike traditional optical or electrical techniques, LIMAS enables simultaneous detection of both radiative and non-radiative recombination while avoiding parasitic effects from electrodes^{28, 29}. We first establish the theoretical framework of LIMAS and then validate

its efficacy by testing two ZnS single crystals. Our results show that the total recombination rate in zinc sulfide follows a multiplicative weighting model, $r_{total} \propto \prod r_i^{w_i}$ with $\sum w_i = 1$, rather than the conventional additive model, providing direct evidence of competitions between recombination pathways.

Theoretical framework of LIMAS

Fig. 1 illustrates the theoretical framework of LIMAS. In a uniformly illuminated yet mechanically static homogeneous compound semiconductor, conduction band electrons ($n = n_0 + \Delta n$), valence band holes ($p = p_0 + \Delta p$), and localized states electrons remain uniformly distributed throughout the bulk sample (Fig. 1b). Here, n_0 and p_0 are thermal equilibrium carrier concentrations, Δn and Δp denote photo-generated excess carriers, and A , B , and C denote different regions of the sample (Fig. 1a). Under this condition, no drift or diffusion current occurs. However, when the sample vibrates at one of its piezoelectrically active resonant eigenmodes (Supplementary Note 3³⁰), piezoelectricity induces a weak internal alternating potential (10^{-9} - 10^{-7} V), perturbing the electron and hole concentrations ($\Delta n'$ and $\Delta p'$, Fig. 1c). This perturbation generates an internal alternating current, leading to mechanical damping (Q^{-1}) and resonance frequency change ($\Delta f_r/f_r$)^{31, 32}, which can be expressed as follows (see Supplementary Note 4 for derivation³⁰):

$$Q^{-1} = \frac{e^2}{c\varepsilon} \frac{\omega_c / \omega}{1 + (\omega_c / \omega)^2}, \quad \frac{\Delta f_r}{f_r} = -\frac{e^2}{2c\varepsilon} \frac{(\omega_c / \omega)^2}{1 + (\omega_c / \omega)^2} \quad (1)$$

where c , e , and ε are the elastic, piezoelectric and dielectric constants, respectively. $\omega = 2\pi f_r$ represents the mechanical vibration frequency and can be considered constant during tests since $\Delta f_r/f_r \ll 1$. $\omega_c = q(\mu_n \Delta n + \mu_p \Delta p)/(f\varepsilon)$ is the conductivity frequency, with μ_n , μ_p as carrier mobilities, q as the elementary charge, and f as the fraction of net space charge contributed by mobile carriers.

For semiconductors under steady-state illumination with a single given recombination pathway, the recombination rate $r = \alpha\beta\Phi \propto (\Delta n)^\gamma$. Where Φ is the photon flux, α and β denote the absorption coefficient and quantum yield. The recombination index γ takes values of 3, 2, 1, and

<1 for Auger, direct, trap-assisted, and sublinear recombination, respectively (Supplementary Note 5³⁰). Trap-assisted recombination, also known as Shockley-Read-Hall recombination^{8,9}, occurs via a single unsaturated defect level (i.e., recombination center, RC, in Fig. 1d), whereas sublinear recombination involves multiple saturated defect levels^{10,33}. Fig. 1e shows the calculated steady-state photon flux-damping curves ($\Phi-Q^{-1}$) and photon flux-resonance frequency change curves ($\Phi-\Delta f_r/f_r$) for each individual recombination pathway, based on Eq.(1) (see Supplementary Note 6 for calculation parameters³⁰). All curves exhibit standard anelastic behavior: the $\Phi-Q^{-1}$ curves follow a Lorentzian peak shape, with the characteristic width (γ) representing the detailed recombination pathway, and the peak position (Φ_p) indicating the recombination rate. A peak shift to higher photon flux suggests an increased recombination rate, and vice versa. Meanwhile, the $\Phi-\Delta f_r/f_r$ curves display a sigmoidal transition from the unrelaxed to the relaxed state. Under transient illumination with a single given recombination pathway, the time-dependent Q^{-1} can also be calculated by first solving the rate equation: $\frac{d\Delta n}{dt} = -r + \alpha\beta\Phi$, and then substituting the resulting $\Delta n(t)$ into Eq. (1).

In practical semiconductors, multiple recombination pathways coexist. If these pathways operate independently, the total recombination rate follows the conventional additive model¹⁹, $r_{total} = \sum r_i$, leading to deviations from standard anelastic behavior in both $\Phi-Q^{-1}$ and $\Phi-\Delta f_r/f_r$ curves. However, if perfect anelasticity is maintained, evidenced by $\Phi-Q^{-1}$ curves consistently exhibiting a perfect Lorentzian peak—it indicates that r_{total} strictly follows a power-law relationship with Δn , and can be described by the multiplicative weighting model:

$$\begin{cases} r_{total} \propto \prod r_i^{w_i}, & \sum w_i = 1, \quad w_i \in [0,1] \\ r_i \propto \Delta n^\gamma, & \gamma = 3, 2, 1, \text{ and } < 1 \text{ for Auger, direct, trap-assisted, and sublinear} \end{cases} \quad (2)$$

where w_i is the weighting factor for each individual recombination pathway (e.g., Auger, direct, trap-assisted, sublinear recombination, and so on) and varies with external conditions such as photon energy and temperature.

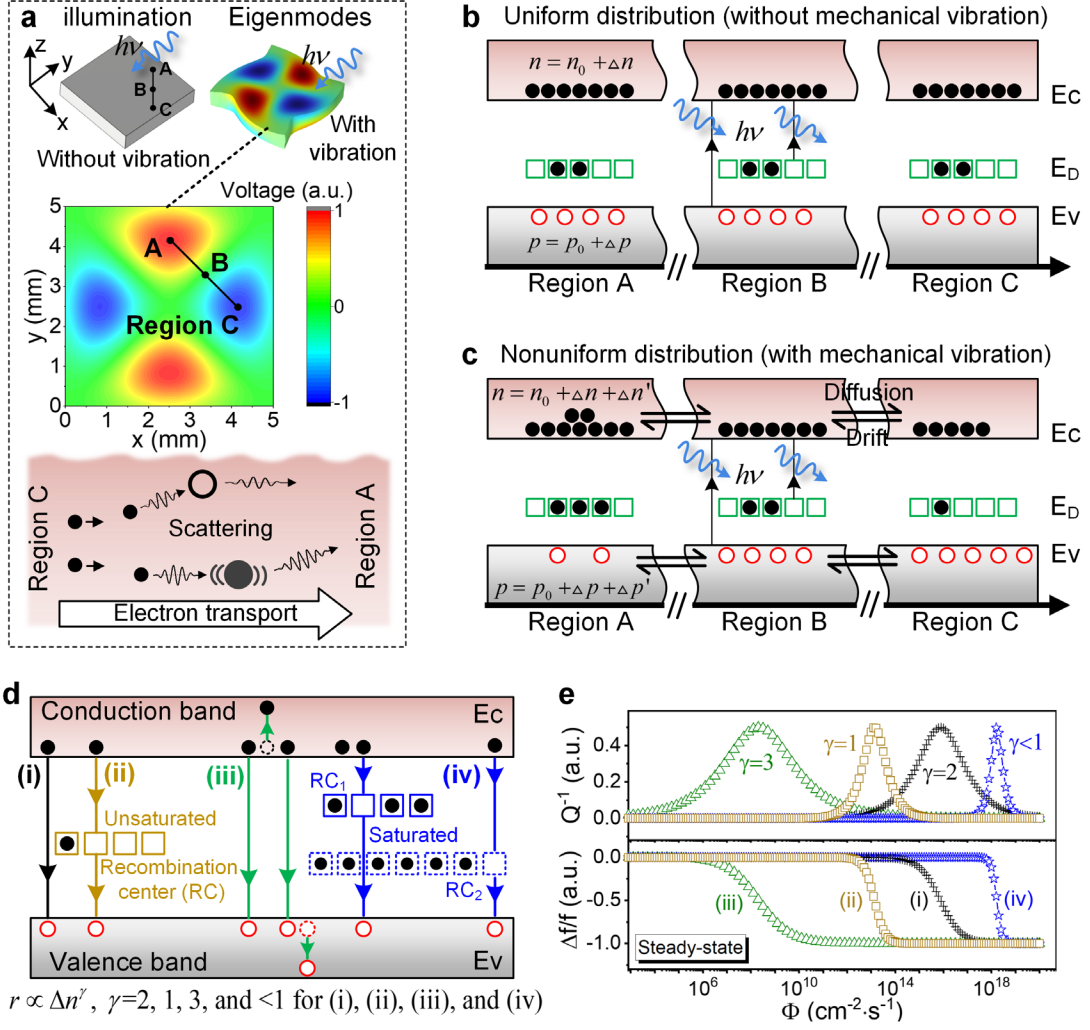


Fig. 1: Theoretical framework of LIMAS for probing recombination dynamics in compound

semiconductors. a, Alternating potentials and carrier transport in a uniformly illuminated compound semiconductor under piezoelectrically active resonant eigenmodes. **b and c**, Distributions of conduction band electrons (black dots), valence band holes (red hollow dots), and localized states electrons across different regions (A, B, and C) of the sample without and with mechanical vibration. **d**, Power-law relationship between recombination rate (r) and carrier concentration (Δn) under steady-state illumination for each individual recombination pathway: (i) Direct, $r \propto \Delta n^2$; (ii) Trap-assisted, $r \propto \Delta n$; (iii) Auger, $r \propto \Delta n^3$; (iv) Sublinear, $r \propto \Delta n^\gamma$, $\gamma \in (0,1)$. **e**, Calculated steady-state photon flux-damping curves ($\Phi-Q^{-1}$) and photon flux-resonance frequency change curves ($\Phi-\Delta f_r/f_r$) for each individual recombination pathway, where γ is the exponent of the recombination rate r and determines the characteristic width of the $\Phi-Q^{-1}$ curve.

Recombination pathways competition under steady-state illumination

To prove the competition between recombination pathways, we perform LIMAS tests on two high-purity cubic zinc sulfide (ZnS) single crystals, denoted as ZnS (i) and (ii), grown under Zn-rich and S-rich conditions, respectively. These crystals were exposed to steady-state monochromatic light with wavelength (λ) ranging from 320 nm to 500 nm and photon flux (Φ) spanning $10^{11} \text{ cm}^{-2} \cdot \text{s}^{-1}$ to $10^{18} \text{ cm}^{-2} \cdot \text{s}^{-1}$. The mechanical damping (Q^{-1}) and resonance frequency change (Δf_r) of the samples were measured using resonant ultrasound spectroscopy³⁴ (RUS) at a resonant frequency (f_r) of approximately 420 kHz (Supplementary Note 2 and 7³⁰). Fig. 2a, b and d, e show that the measured Φ - Q^{-1} and Φ - Δf_r curves maintain perfect anelastic responses (show Lorentzian peak and sigmoidal transition, Supplementary Note 8³⁰) across various wavelengths, providing direct evidences for the multiplicative weighting model and recombination pathways competition. Fitting the Φ - Q^{-1} curves using the multiplicative weighting model (see Supplementary Note 8 for fitting details and a comparison with additive model fitting³⁰) yields the photon flux at the damping peak (Φ_p) and the corresponding γ values, as shown in Fig. 2c and f. When the photon energy exceeds the bandgap energy ($E_g = 3.6 \text{ eV}$, $\sim 345 \text{ nm}$, Fig. 2h), intrinsic absorption and interband transitions dominate. In this regime, the γ values for both ZnS (i) and (ii) gradually approach 2, indicating an increasing weighting factor for direct recombination (i.e., w_{direct} increases). Auger recombination is ruled out here, as it primarily occurs in heavily doped semiconductors. The inferred recombination mechanisms, based on the extracted γ values, are annotated in Fig. 2c, f and g, with larger font sizes representing greater weighting factors.

Under extrinsic absorption, the recombination behaviors differ. For ZnS (i) in the 365 nm-425 nm illumination range, carrier generation is primarily mediated by a single defect energy level. Both γ and Φ_p remain stable at approximately 1.2 and $1.5 \times 10^{14} \text{ cm}^{-2} \cdot \text{s}^{-1}$, respectively, suggesting unchanged w_i . According to the multiplicative weighting model, trap-assisted recombination dominates in this regime with a weighting factor $w_{trap} \approx 0.8$, while direct recombination (w_{direct}) contributes ≈ 0.2 . As the monochromatic light shifts beyond 440 nm but remains below 520 nm, γ drops below 1, and the damping peak shifts rapidly toward higher photon flux. This indicates the onset and progressive enhancement of sublinear recombination (i.e., w_{sub} increases).

Photoluminescence contour map of ZnS (i) in Fig. 2g further confirms the variation of w_i with photon energies, and attribute the observed green light emission (~520 nm) to trap-assisted recombination. Compared to ZnS (i), ZnS (ii) exhibits slightly larger Φ_p and γ values under extrinsic absorption (Fig. 2f). Fig. 2g and h show that ZnS (ii) has weaker green emission and lower absorption coefficients, indicating a lower concentration of specific intrinsic defects. DFT calculations (Supplementary Note 13³⁰) identify this defect as the zinc antisite (Zn_S), which introduces a deep level within the bandgap, serving as the recombination center that facilitates trap-assisted and sublinear recombination. Consequently, in ZnS (ii), these defect-related recombination processes are weaker, while direct recombination remains a non-negligible competitor under extrinsic absorption, resulting in observed larger Φ_p and γ .

To better illustrate the competition between recombination pathways, we present a curved surface in cylindrical coordinates to visualize the multiplicative weighting model, with trap-assisted and direct recombination as an example (Fig. 2i). Here, r denotes the total recombination rate, $\theta \in [0, \pi/2]$ determines the weighting factors ($w_{direct} = \cos^2\theta$, and $w_{trap} = \sin^2\theta$), and z represents the carrier concentration Δn . As the photon energy decreases and falls slightly below E_g , θ varies from 0 to $\pi/2$, and the r - Δn relationship shifts from a parabola to a linear form, reflecting the continuous transition from direct to trap-assisted recombination.

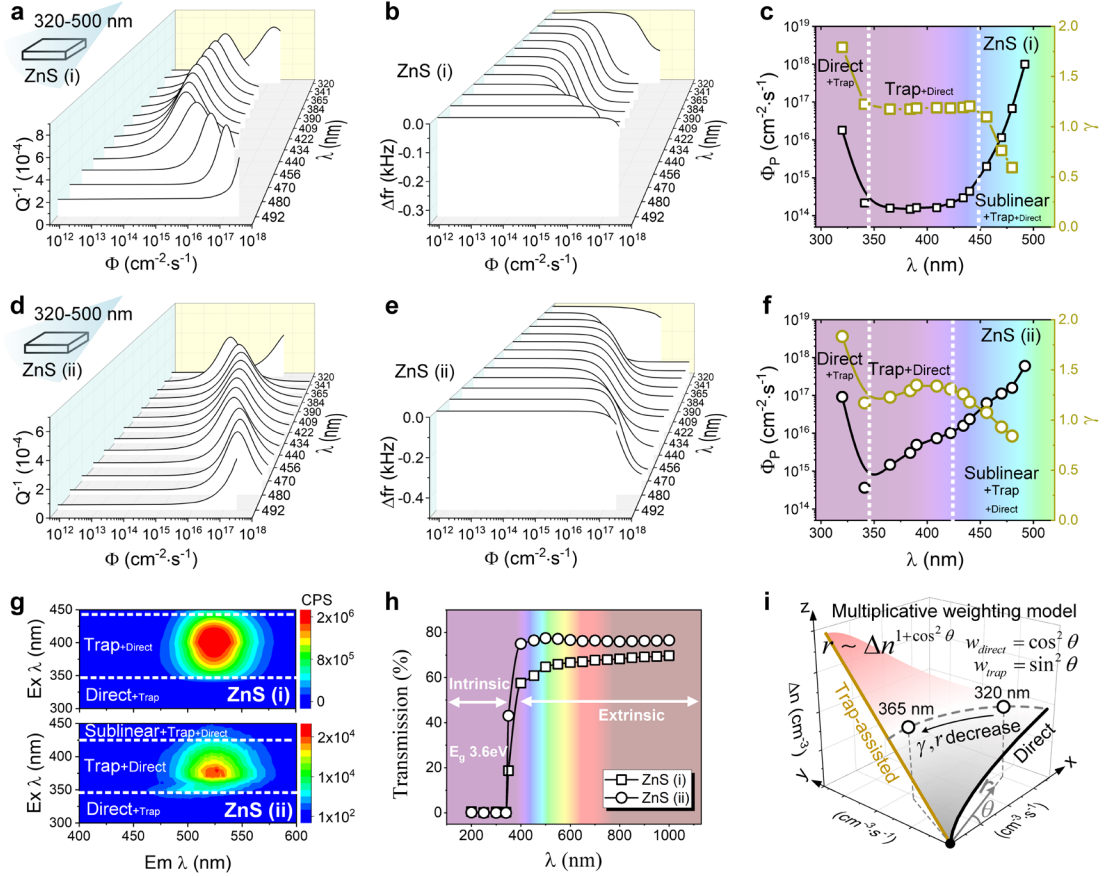


Fig. 2: Responses of ZnS to steady-state monochromatic light. **a, b** and **d, e**, Photon flux-damping curves ($\Phi-Q^{-1}$) and photon flux-resonance frequency change curves ($\Phi-\Delta f_r$) of ZnS (i) and (ii) under steady-state monochromatic light with varying wavelengths (λ). **c** and **f**, Photon flux at the damping peak (Φ_p), characteristic width (γ) of the damping peak, and the inferred recombination mechanisms based on γ , for ZnS (i) and (ii) under monochromatic light with different wavelengths (λ). **g**, Photoluminescence contour maps of ZnS (i) and (ii), with excitation wavelengths ($E_x \lambda$) ranging from 300 nm to 450 nm and detected emission wavelengths ($E_m \lambda$) from 400 nm to 600 nm. **h**, Transmission spectra of ZnS (i) and (ii). **i**, Graphical representation of the multiplicative weighting model as a curved surface in cylindrical coordinates, illustrating the competition between direct and trap-assisted recombination in ZnS. Here, r , θ , and z determine the total recombination rate, weighting factors, and carrier concentration, respectively.

We introduce a second light source to examine its effect on the weighting factor w_i established under monochromatic light. Here, a constant-intensity 365 nm UV light combined with an additional light source (400 nm–1100 nm) with varying photon flux $\Phi_{additional}$ ($10^{12} \text{ cm}^{-2} \cdot \text{s}^{-1}$ to $10^{17} \text{ cm}^{-2} \cdot \text{s}^{-1}$) is applied (Fig. 3a-d). The 365 nm UV light serves as the background because it mainly induces trap-assisted recombination (Fig. 2c and f), and the additional light influences only this pathway, as evidenced by the photoluminescence quenching contour map in Supplementary Note 10³⁰. The UV light establishes the baseline $\Delta n/\Delta p$, Q^{-1} , and Δf_r (hollow dots in Fig. 3a), while the additional light induces two opposite effects: (1) Injection, which increases $\Delta n/\Delta p$, thereby reducing both Q^{-1} and Δf_r (blue arrows). (2) Quenching^{33, 35}, which decreases $\Delta n/\Delta p$, restoring Q^{-1} and Δf_r (red arrows). Fig. 3b-d present the Q^{-1} and photoluminescence responses of ZnS. In ZnS (i), the additional light below 440 nm induces only injection (Fig. 3b). Between 440 and 500 nm, injection and quenching compete, producing peaks in both the Q^{-1} and Δf_r curves (Supplementary Note 11³⁰). Beyond 520 nm, quenching dominates, recovering Q^{-1} , increasing Δf_r (Supplementary Note 11³⁰), reducing green light emission³⁵, and generating a weak orange light emission (Fig. 3d). ZnS (ii) follows similar trends, but quenching occurs at a shorter wavelength (~430 nm, Fig. 3c).

By correlating the characteristic wavelengths at which quenching (Fig. 3b and c) and sublinear recombination (Fig. 2c and f) occur, we infer that quenching results from the onset of sublinear recombination. This process reduces w_{trap} while increasing w_{sub} , altering light emission, increasing r_{total} . To further validate this, damping contour maps (Fig. 3e) were recorded for ZnS (i). The results show that quenching, represented by the ‘bending’ in the contour maps, coincides with the damping peak narrowing (γ decreases), reflecting the onset and progressive enhancement of sublinear recombination. Moreover, the narrowed damping peaks retain perfect Lorentzian shapes (see waterfall plot in Fig. 3f and Supplementary Note 8³⁰), confirming that r_{total} still adhere to the multiplicative weighting model under bichromatic illumination. Fig. 3g visualizes the competition between trap-assisted and sublinear recombination. As the photon energy of monochromatic light decreases from E_g to $0.66E_g$ - $0.8E_g$, or with the addition of long-wavelength light ($<0.8E_g$), θ shifts from $\pi/2$ to π , increasing w_{sub} , while decreasing w_{trap} . Consequently,

the r - Δn relationship transitions from a linear trend (trap-assisted) to a root curve (sublinear).

Fig. 3h-j illustrate the detailed electron behaviors underlying the competition between trap-assisted and sublinear recombination in ZnS. Under 365 nm UV light, recombination center 1 (RC₁, identified as the zinc antisite through DFT calculations, Supplementary Note 13³⁰) facilitates carrier generation, trap-assisted recombination, and green light emission. While other defect levels, RC₂ (sulfur vacancy, Supplementary Note 13³⁰), remains fully occupied and does not participate in the recombination process (Fig. 3h). Introducing additional light in the 365 nm-440 nm range increases $\Delta n/\Delta p$ and enhances green light emission, without altering the recombination pathway. However, illumination in the 440 nm-520 nm range triggers electron redistribution between RC₁ and RC₂. Since RC₂ is more abundant than RC₁, electrons gradually saturate both centers, altering the carrier generation mechanism. This process reduces trap-assisted recombination, initiates sublinear recombination (Fig. 3i), reduces green emission, and induces weak orange emission. As both recombination centers become activated, r_{total} increases, initially reducing Δn (Fig. 3i, left). However, because 440 nm-520 nm light also contributes to carrier generation, increasing photon flux eventually raises Δn (Fig. 3i, right), resulting in peaks in both the Q^{-1} and Δf_r curves (Fig. 3b and c). Beyond 520 nm, electron redistribution between RC₁ and RC₂ continues, but in the absence of additional carrier generation, Δn steadily decreases (Fig. 3j).

Analysis of the weighting factors w_i for each recombination pathway under the steady-state monochromatic and bichromatic illuminations reveals a key conclusion: electron-hole pairs preferentially recombine through their original generation pathways. Specifically, for photon energies above the bandgap ($E_{photon} > E_g$), interband transitions dominate, promoting direct recombination (increasing w_{direct} , the weighting factor of direct recombination). Slightly below the bandgap ($0.8E_g - E_g$), carrier generation is primarily governed by a single defect energy level, favoring trap-assisted recombination (increasing w_{trap}). At much lower energies ($0.66E_g - 0.8E_g$) or under additional long-wavelength illumination ($< 0.8E_g$), electron saturates multiple defect levels, giving rise to sublinear recombination (increasing w_{sub}).

Recombination pathways competition under transient illumination

Under steady-state illumination, recombination pathways in ZnS exhibit strong competition, with the total recombination rate r_{total} following a multiplicative weighting model. To study transient processes, the time dependence of Q^{-1} in ZnS (i) were measured during abrupt switching on/off of monochromatic light (320 nm, 365 nm, 456 nm, and 470 nm) and bichromatic light (365 nm + 800 nm, where the 800 nm light maintains open status and only the 365 nm light is switched, $\Phi_{800} = 10^{16} \text{ cm}^{-2} \cdot \text{s}^{-1}$), as shown in Fig. 4a, b. The curves maintain a constant Q^{-1} in both the initial and final states, ensuring a consistent carrier concentration under each illumination condition. r_{total} , inversely proportional to the time required for Q^{-1} to reach equilibrium, strongly depends on the photon energy. At 320 nm, r_{total} is slightly higher than at 365 nm due to increased direct recombination weighting factor (w_{direct}), aligning with the observed damping peak shift in the intrinsic absorption region under steady-state (Fig. 2c). Similarly, at 470 nm and 365 nm + 800 nm, r_{total} is significantly larger than at 365 nm due to the increased weighting factor of sublinear recombination (w_{sub}), also consistent with the steady-state observations (Fig. 2c and 3f). This indicates that pathway competition persists even in the transient processes.

To further validate the multiplicative weighting model and determine whether w_i changes during transient processes, switch-on/off curves at 365 nm at varying photon flux (Φ) were measured (hollow squares in Fig. 4c and d) and compared with numerical solutions (solid lines) derived from the rate equations: $\frac{d\Delta n}{dt} = -c_{total} \cdot \Delta n^\gamma + \alpha\beta\Phi$ (switch-on), and $\frac{d\Delta n}{dt} = -c_{total} \cdot \Delta n^\gamma$ (switch-off). Where $\gamma = 1.2$ and $c_{total} = 3.83 \times 10^{-4} \text{ cm}^{0.6} \cdot \text{s}^{-1}$ are determined from the steady-state results (see Supplementary Note 12 for details³⁰). The strong agreement between numerical predictions and experimental data for the switch-on process (see Supplementary Note 12 for additional results³⁰) further supports the multiplicative weighting model, reflecting a constant- θ trajectory in Fig. 4e, indicating that w_i remains unchanged during switch-on. However, during switch-off, the numerically predicted recombination rate falls significantly below the experimental values. The corresponding time-dependent light emissions also decay more rapidly during switch-off than they rise during switch-on (the contour maps in Fig. 4c and d). These discrepancies suggest

that during switch off, w_i evolves dynamically rather than remaining constant, as shown by the inferred θ -changing trajectory in Fig. 4e. Specifically, upon turning off the 365 nm light, carriers initially undergo direct recombination due to localized state changes, resulting in a higher recombination rate (State (i) in Fig. 4e). This is subsequently followed by a transition to trap-assisted recombination, which proceeds at a lower rate (State (ii) in Fig. 4e).

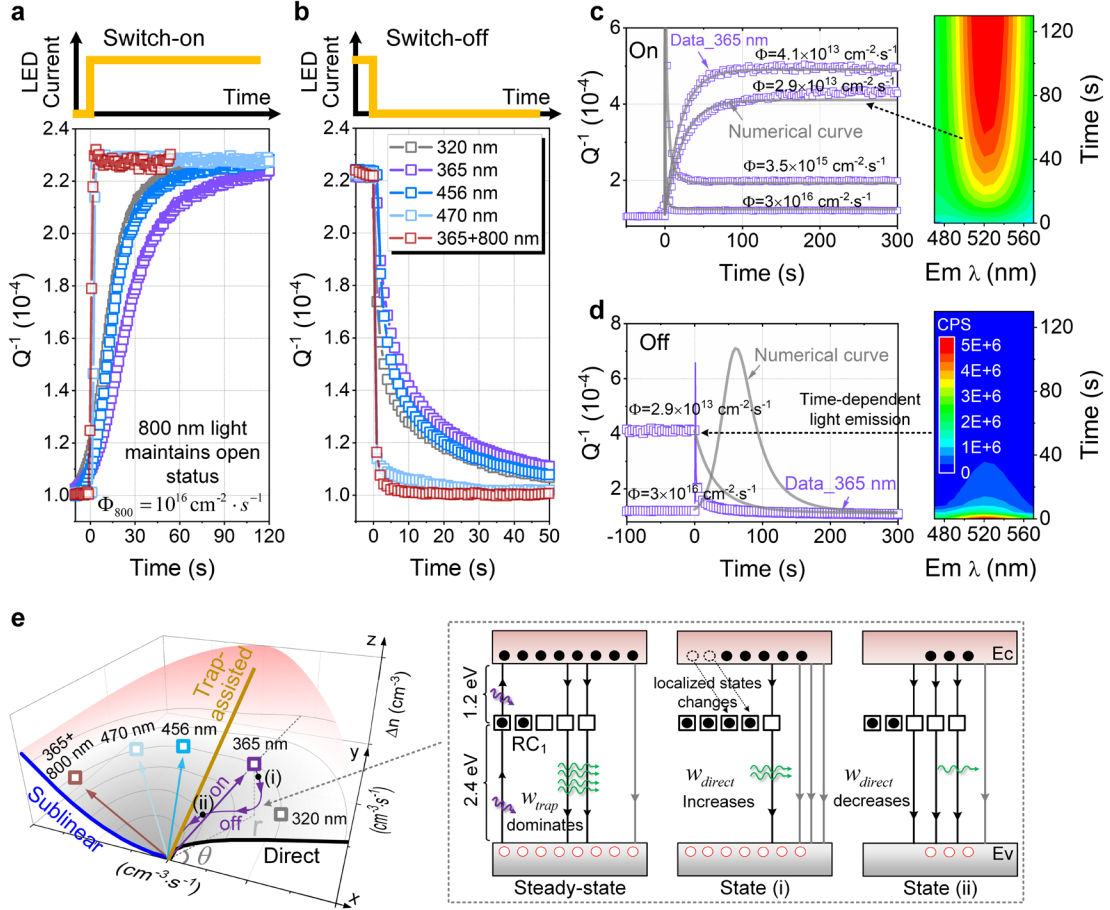


Fig. 4: Responses of ZnS (i) to transient illumination. **a and b**, Time dependence of Q^{-1} during abrupt switching-on/off of monochromatic light (320 nm, 365 nm, 456 nm, and 470 nm) and bichromatic light (365 nm + 800 nm, where the 800 nm light maintains open status and only the 365 nm light is switched, $\Phi_{800} = 10^{16} \text{ cm}^{-2} \cdot \text{s}^{-1}$). **c and d**, Measured and numerically calculated (assuming constant w_i) time dependence of Q^{-1} during switching on/off of 365 nm light at various photon flux. The corresponding time-dependent light emissions were also recorded. **e**, Graphical representation of the switch-on/off processes. During switch-on, θ remains constant, indicating unchanged w_i ; during switch-off, localized state changes drive a dynamic evolution of w_i , altering pathway competitions.

Summary and Outlook

In this work, we develop light-induced mechanical absorption spectroscopy (LIMAS) and, for the first time, provide direct evidence of competitions between recombination pathways in bulk semiconductors. Our results demonstrate that the total recombination rate in ZnS follows a multiplicative weighting model, $r_{total} \propto \prod r_i^{w_i}$ with $\sum w_i = 1$. Under steady-state and switch-on conditions, the weighting factors w_i are governed by the carrier generation mechanism: the interband transition favors direct recombination (increasing w_{direct}), single-defect level-mediated generation promotes trap-assisted recombination (increasing w_{trap}), and generation involving multiple saturated defect levels gives rise to sublinear recombination (increasing w_{sub}). During switch-off, w_i evolves dynamically in response to localized state changes. Our findings reshape the fundamental understanding of carrier dynamics and provide new opportunities for the following applications:

We demonstrate that the recombination pathway in semiconductors can be selectively enhanced or suppressed by tailoring carrier generation, either through external stimulus (e.g., photon energy, temperature) or defect engineering. This enables new strategies for optimizing optoelectronic devices. For example, in LEDs^{1, 5}, where emission efficiency relies on direct band-to-band recombination, stronger interband excitation should be promoted. In photodetectors, enhancing saturated defect levels-mediated carrier generation, which drives sublinear recombination, can improve both sensitivity and image contrast^{2, 16, 36}. Moreover, precise control over recombination dynamics during switching processes offers a promising route to mitigate persistent photoconductivity³⁷ and memory effects³⁸ in resistive switching devices.

LIMAS has the potential to become a powerful, broadly applicable technique for probing complex recombination processes in a wide variety of semiconductors. Its capabilities can be significantly expanded by integration with complementary methods and multi-physics approaches. For example, combining LIMAS with power-dependent/time-resolved photoluminescence¹⁵ enables non-contact, quantitative separation of radiative and non-radiative recombination processes, facilitating defect-

related loss analysis and the optimization of light-emitting devices. Applying magnetic or electric fields during LIMAS measurements allows for an independent assessment of minority and majority carrier properties³⁹, providing deep insights into field-modulated trapping and recombination dynamics^{40, 41}. Enhancing LIMAS's time resolution by replacing the resonance-based method with surface acoustic waves (SAWs, GHz range) would enable studies of ultrafast phenomena such as hot carrier relaxation⁴² and exciton dynamics¹¹, while also extending its applicability to thin films and 2D semiconductors⁴³. Finally, adopting contact-resonance damping detection methods, such as atomic force microscopy (AFM)⁴⁴, could significantly improve LIMAS's spatial resolution, enabling the investigation of recombination behavior at the level of individual defects, such as dislocations⁴⁵ and stacking faults⁴⁶.

Materials and Methods

Single-crystal samples

Two high-purity cubic ZnS single crystals, labeled ZnS (i) and (ii), were synthesized using a modified Bridgman technique in Zn-rich and S-rich environments, respectively. The samples were cut into wafers measuring approximately 10mm×10mm×1mm and polished to optical-grade smoothness. The thickness of the wafers was aligned with the (110) crystallographic plane.

Light-induced mechanical absorption spectroscopy (LIMAS)

Q^{-1} and Δf_r were measured under different illumination conditions using resonant ultrasound spectroscopy³⁴ (RUS, Alamo Creek Engineering). The ZnS sample was clamped between the two opposite corners of two PZT transducers. The transmitting transducer generated elastic waves with constant amplitude across a frequency range from kHz to MHz. When the excitation frequency coincided with one of the sample's eigenfrequencies, the receiving transducer picked up a significant peak in the amplitude-frequency curve. The Q^{-1} value was calculated from the peak's half-bandwidth (-3 dB), while f_r was determined from its position. For illumination, various LEDs with emission wavelengths ranging from 320 nm to 1000 nm were used. The photon flux was measured

with a Si-based photodiode power sensor (S120VC, Thorlabs). A LabVIEW program is employed to control all the components of the setup.

Photoluminescence spectra

Photoluminescence contour maps (Fig. 2g) were measured using a Horiba spectrofluorometer (FluoroMax Plus) equipped with a xenon lamp as the excitation source. Measurements were conducted at room temperature with a 2 nm emission step size, 5 nm excitation step size, 0.1 s integration time, and (2×2) entrance and exit slits. For time-dependent light emission measurements (Fig. 4c and d), a 365 nm LED was used as the excitation source, and the spectrofluorometer recorded the emission during the switching on/off of the LED.

Transmission spectra

A Lambda 365 Spectrometer was used to measure optical transmission between 200 nm and 1000 nm. The measurements were carried out at room temperature, with a 5 nm interval, 0.1 s integration time, and 2.0 nm bandwidth.

Data availability

The data that support the findings of this study are available from the corresponding author upon reasonable request.

Acknowledgements

We acknowledge the financial support from the Discovery Grants Program of the Natural Sciences and Engineering Research Council of Canada (NSERC) RGPIN-2018-05731, the Ontario Early Researcher Award, and the Canada Foundation for Innovation (CFI) - Evans Leaders Fund (JELF) Number 38044.

Author contributions

Mingyu Xie: Conceptualization, Methodology, Investigation, Data curation, Writing–original draft, Writing–review & editing. **Ruitian Chen:** Conceptualization, Methodology, Investigation, Writing–review & editing. **Jiaze Wu:** Methodology, Investigation, Writing–review & editing. **Kaiqi Qiu:** Investigation, Writing–review & editing. **Mingqiang Li:** Investigation, Writing–review & editing. **Huicong Chen:** Investigation, Writing–review & editing. **Kai Huang:** Conceptualization, Supervision, Writing–review & editing. **Yu Zou:** Conceptualization, Funding acquisition, Supervision, Writing–review & editing.

Competing interests

There is no conflict of interest to declare.

References

1. Pimputkar S, Speck JS, DenBaars SP, Nakamura S. Prospects for LED lighting. *Nature photonics* 2009, **3**(4): 180-182.
2. Fang Y, Dong Q, Shao Y, Yuan Y, Huang J. Highly narrowband perovskite single-crystal photodetectors enabled by surface-charge recombination. *Nature Photonics* 2015, **9**(10): 679-686.
3. Mora-Seró I, Bisquert J. Breakthroughs in the development of semiconductor-sensitized solar cells. *The journal of physical chemistry letters* 2010, **1**(20): 3046-3052.
4. Odunmbaku GO, Chen S, Guo B, Zhou Y, Ouedraogo NAN, Zheng Y, *et al.* Recombination pathways in perovskite solar cells. *Advanced Materials Interfaces* 2022, **9**(12): 2102137.
5. Olivier F, Daami A, Licitra C, Templier F. Shockley-Read-Hall and Auger non-radiative recombination in GaN based LEDs: A size effect study. *Applied Physics Letters* 2017, **111**(2).
6. Bae WK, Park Y-S, Lim J, Lee D, Padilha LA, McDaniel H, *et al.* Controlling the influence of Auger recombination on the performance of quantum-dot light-emitting diodes. *Nature communications* 2013, **4**(1): 2661.

7. Peng W, Mao K, Cai F, Meng H, Zhu Z, Li T, *et al.* Reducing nonradiative recombination in perovskite solar cells with a porous insulator contact. *Science* 2023, **379**(6633): 683-690.
8. Shockley W, Read Jr W. Statistics of the recombinations of holes and electrons. *Physical review* 1952, **87**(5): 835.
9. Hall RN. Electron-hole recombination in germanium. *Physical Review* 1952, **87**(2): 387.
10. Rose A. Recombination processes in insulators and semiconductors. *Physical Review* 1955, **97**(2): 322.
11. Koch S, Kira M, Khitrova G, Gibbs H. Semiconductor excitons in new light. *Nature materials* 2006, **5**(7): 523-531.
12. Strauss U, Rühle W, Köhler K. Auger recombination in intrinsic GaAs. *Applied Physics Letters* 1993, **62**(1): 55-57.
13. Sah C-T, Noyce RN, Shockley W. Carrier generation and recombination in pn junctions and pn junction characteristics. *Proceedings of the IRE* 2007, **45**(9): 1228-1243.
14. Ravensbergen J, Abdi FF, Van Santen JH, Frese RN, Dam B, Van De Krol R, *et al.* Unraveling the carrier dynamics of BiVO₄: a femtosecond to microsecond transient absorption study. *The Journal of Physical Chemistry C* 2014, **118**(48): 27793-27800.
15. Gilliland G. Photoluminescence spectroscopy of crystalline semiconductors. *Materials Science and Engineering: R: Reports* 1997, **18**(3-6): 99-399.
16. Binet F, Duboz J, Rosencher E, Scholz F, Härle V. Mechanisms of recombination in GaN photodetectors. *Applied physics letters* 1996, **69**(9): 1202-1204.
17. Li B-H, Li H, Di H, Xuan Z, Zeng W, Wang J-C, *et al.* Probing the genuine carrier dynamics of semiconducting perovskites under sunlight. *Jacs Au* 2023, **3**(2): 441-448.
18. Kaiser M, Li Y, Allegro I, Richards BS, Paetzold UW, Howard IA. Interpreting the Time-Resolved Photoluminescence of Quasi-2D Perovskites. *Advanced Materials Interfaces* 2021, **8**(24): 2101326.

19. Shen Y, Mueller G, Watanabe S, Gardner N, Munkholm A, Krames M. Auger recombination in InGaN measured by photoluminescence. *Applied Physics Letters* 2007, **91**(14).
20. Chen W, Huang Z, Yao H, Liu Y, Zhang Y, Li Z, *et al.* Highly bright and stable single-crystal perovskite light-emitting diodes. *Nature Photonics* 2023, **17**(5): 401-407.
21. Kiligaridis A, Frantsuzov PA, Yangui A, Seth S, Li J, An Q, *et al.* Are Shockley-Read-Hall and ABC models valid for lead halide perovskites? *Nature communications* 2021, **12**(1): 3329.
22. Feldmann S, Macpherson S, Senanayak SP, Abdi-Jalebi M, Rivett JP, Nan G, *et al.* Photodoping through local charge carrier accumulation in alloyed hybrid perovskites for highly efficient luminescence. *Nature Photonics* 2020, **14**(2): 123-128.
23. Stranks SD, Burlakov VM, Leijtens T, Ball JM, Goriely A, Snaith HJ. Recombination kinetics in organic-inorganic perovskites: excitons, free charge, and subgap states. *Physical Review Applied* 2014, **2**(3): 034007.
24. Johnston MB, Herz LM. Hybrid perovskites for photovoltaics: charge-carrier recombination, diffusion, and radiative efficiencies. *Accounts of chemical research* 2016, **49**(1): 146-154.
25. Singha PK, Mukhopadhyay T, Tarif E, Ali F, Datta A. Competition among recombination pathways in single FAPbBr₃ nanocrystals. *The Journal of Chemical Physics* 2024, **161**(5).
26. Mangum BD, Wang F, Dennis AM, Gao Y, Ma X, Hollingsworth JA, *et al.* Competition between Auger Recombination and Hot-Carrier Trapping in PL Intensity Fluctuations of Type II Nanocrystals. *Small* 2014, **10**(14): 2892-2901.
27. Yuan G, Gómez DE, Kirkwood N, Boldt K, Mulvaney P. Two mechanisms determine quantum dot blinking. *ACS nano* 2018, **12**(4): 3397-3405.
28. Chen FW, Cotter JE, Abbott MD, Li T-TA, Fisher KC. The influence of parasitic effects on injection-level-dependent lifetime data. *IEEE transactions on electron devices* 2007, **54**(11): 2960-2968.
29. Van Dyk E, Meyer EL. Analysis of the effect of parasitic resistances on the performance of photovoltaic modules. *Renewable energy* 2004, **29**(3): 333-344.
30. Supplementary material.

31. Hutson A, White DL. Elastic wave propagation in piezoelectric semiconductors. *Journal of Applied Physics* 1962, **33**(1): 40-47.
32. White DL. Amplification of ultrasonic waves in piezoelectric semiconductors. *Journal of Applied Physics* 1962, **33**(8): 2547-2554.
33. Bube RH. Infrared quenching and a unified description of photoconductivity phenomena in cadmium sulfide and selenide. *Physical Review* 1955, **99**(4): 1105.
34. Migliori A, Sarrao J, Visscher WM, Bell T, Lei M, Fisk Z, *et al.* Resonant ultrasound spectroscopic techniques for measurement of the elastic moduli of solids. *Physica B: Condensed Matter* 1993, **183**(1-2): 1-24.
35. Huang Z, Mott D, Shu P, Zhang R, Chen J, Wickenden D. Optical quenching of photoconductivity in GaN photoconductors: Materials Research Society, Pittsburgh, PA (United States); 1997.
36. Meng X, Du Y, Wu W, Joseph NB, Deng X, Wang J, *et al.* Giant superlinear power dependence of photocurrent based on layered Ta₂NiS₅ photodetector. *Advanced Science* 2023, **10**(20): 2300413.
37. Lang D, Logan R. Large-lattice-relaxation model for persistent photoconductivity in compound semiconductors. *Physical Review Letters* 1977, **39**(10): 635.
38. Ielmini D, Wong H-SP. In-memory computing with resistive switching devices. *Nature electronics* 2018, **1**(6): 333-343.
39. Musiienko A, Yang F, Gries TW, Frasca C, Friedrich D, Al-Ashouri A, *et al.* Resolving electron and hole transport properties in semiconductor materials by constant light-induced magneto transport. *Nature Communications* 2024, **15**(1): 316.
40. Lepine DJ. Spin-dependent recombination on silicon surface. *Physical Review B* 1972, **6**(2): 436.
41. Leijtens T, Srimath Kandada AR, Eperon GE, Grancini G, D'Innocenzo V, Ball JM, *et al.* Modulating the electron-hole interaction in a hybrid lead halide perovskite with an electric field. *Journal of the American Chemical Society* 2015, **137**(49): 15451-15459.
42. Fu J, Xu Q, Han G, Wu B, Huan CHA, Leek ML, *et al.* Hot carrier cooling

- mechanisms in halide perovskites. *Nature communications* 2017, **8**(1): 1-9.
43. Wixforth A, Kotthaus JP, Weimann G. Quantum oscillations in the surface-acoustic-wave attenuation caused by a two-dimensional electron system. *Physical review letters* 1986, **56**(19): 2104.
 44. Anczykowski B, Gotsmann B, Fuchs H, Cleveland J, Elings V. How to measure energy dissipation in dynamic mode atomic force microscopy. *Applied Surface Science* 1999, **140**(3-4): 376-382.
 45. Figielski T. Recombination at dislocations. *Solid-State Electronics* 1978, **21**(11-12): 1403-1412.
 46. Korona K, Reszka A, Sobanska M, Perkowska P, Wyszomłek A, Klocek K, *et al.* Dynamics of stacking faults luminescence in GaN/Si nanowires. *Journal of luminescence* 2014, **155**: 293-297.

Supplementary Information

Unveiling competitions between carrier recombination pathways in semiconductors via mechanical damping

Mingyu Xie¹, Ruitian Chen¹, Jiaze Wu¹, Kaiqi Qiu¹, Mingqiang Li¹, Huicong Chen¹, Kai Huang¹, Yu Zou^{1,a)}

¹Department of Materials Science and Engineering, University of Toronto, Toronto, ON M5S 3E4, Canada

Supplementary Information	1
Supplementary Note 1. Annotation of symbols	2
Supplementary Note 2. Setup of LIMAS	3
Supplementary Note 3. Piezoelectrically active/inactive eigenmodes	5
Supplementary Note 4. Derivation of Eq. (1)	6
Supplementary Note 5. γ value, damping, and resonance frequency change for each individual recombination pathway	10
Supplementary Note 6. Parameters used to calculate Fig. 1e	12
Supplementary Note 7. Extract damping and resonance frequency from the measured amplitude-frequency curve.....	13
Supplementary Note 8. Fit the photon flux-damping and photon flux-resonance frequency change curve of ZnS using two models	15
Supplementary Note 9. Photon flux-damping and photon flux-resonance frequency change curves for GaN:C and GaAs	18
Supplementary Note 10. Photoluminescence quenching contour maps.....	20
Supplementary Note 11. Resonance frequency change in ZnS under steady-state bichromatic illumination	21
Supplementary Note 12. Calculate time-dependent damping during the transient process	22
Supplementary Note 13. Trap-assisted and sublinear recombination related intrinsic defects	24
References.....	26

^{a)} Author to whom all correspondence should be addressed, Email: mse.zou@utoronto.ca

Supplementary Information

Supplementary Note 1. Annotation of symbols

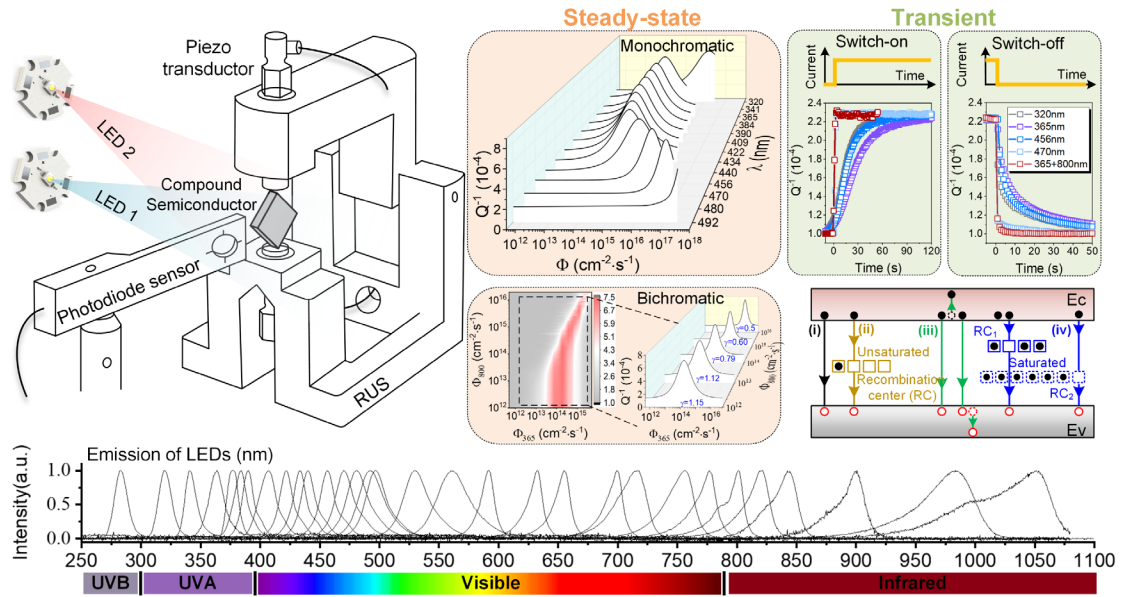
Table 1.1 Annotation of symbols

Symbol	Expressions	Annotations
c		Elastic coefficient
c_n, c_p		Electron and hole capture coefficients of a recombination center
c_D, c_A, c_T, c_S		Coefficient for direct, Auger, trap-assisted and sublinear recombination
D		Electric displacement
D_n, D_p		Diffusion coefficients of electrons and holes
D_{eq}	$\frac{D_n + \eta D_p}{1 + \eta}$	Equivalent diffusion coefficient
E		Electric field
e		Piezoelectric coefficient
f	$\frac{\Delta n' - \Delta p'}{n_{net}}$	The fraction of net space charge contributed by mobile carriers
f_r		Mechanical resonant frequency
g	$\alpha\beta\Phi$	Photogeneration rate
i	$\sqrt{-1}$	Imaginary unit
J_n, J_p		Current in conduction and valence bands
k	ω/v_0	Elastic wavenumber
N_r		Concentration of the recombination center for trap-assisted recombination
n_0, p_0		Thermal equilibrium carrier concentration
$\Delta n, \Delta p$		Photo-generated excess carrier concentration
$\Delta n_0, \Delta n_\infty$		Initial and final photo-generated excess carrier concentration
$\Delta n', \Delta p'$		Perturbation of carrier concentrations induced by elastic vibration
n_{net}	$-\frac{\nabla \cdot D}{q}$	Net space charge concentration
Q^{-1}		Mechanical damping
q		Elementary charge
r_i, r_{total}		Individual and total recombination rate
S, T		Strain and stress
t, u		Time and displacement
v_0	$\sqrt{c/\rho}$	Elastic wave velocity
w_i		Weighting factor of each pathway (w_{direct} , w_{trap} , and w_{sub} in this work)
α, β		Absorption coefficient and quantum yield
γ		Index, $\gamma=3,2,1,<1$ for Auger, direct, trap-assisted and sublinear recombination
ϵ		Dielectric coefficient
η	$-\Delta p'/\Delta n'$	The ratio of $\Delta p'$ to $\Delta n'$
λ		The wavelength of light
μ_n, μ_p		Electron and hole mobility

Supplementary Information

ρ		Mass density
σ	$q(\mu_n n + \mu_p p)$	Conductivity
τ_n, τ_p		Lifetimes of electrons and holes
τ_{eq}	$\frac{1 + \eta}{\frac{\eta}{\tau_p} + \frac{1}{\tau_n}}$	Equivalent lifetime
τ_T	$\frac{c_n + c_p}{c_n c_p N_r}$	Lifetime of trap-assisted recombination
Φ		Photon flux
$\omega, \omega_c, \omega_D, \omega_\tau$		Mechanical, conductivity, diffusion, and lifetime frequency

Supplementary Note 2. Setup of LIMAS



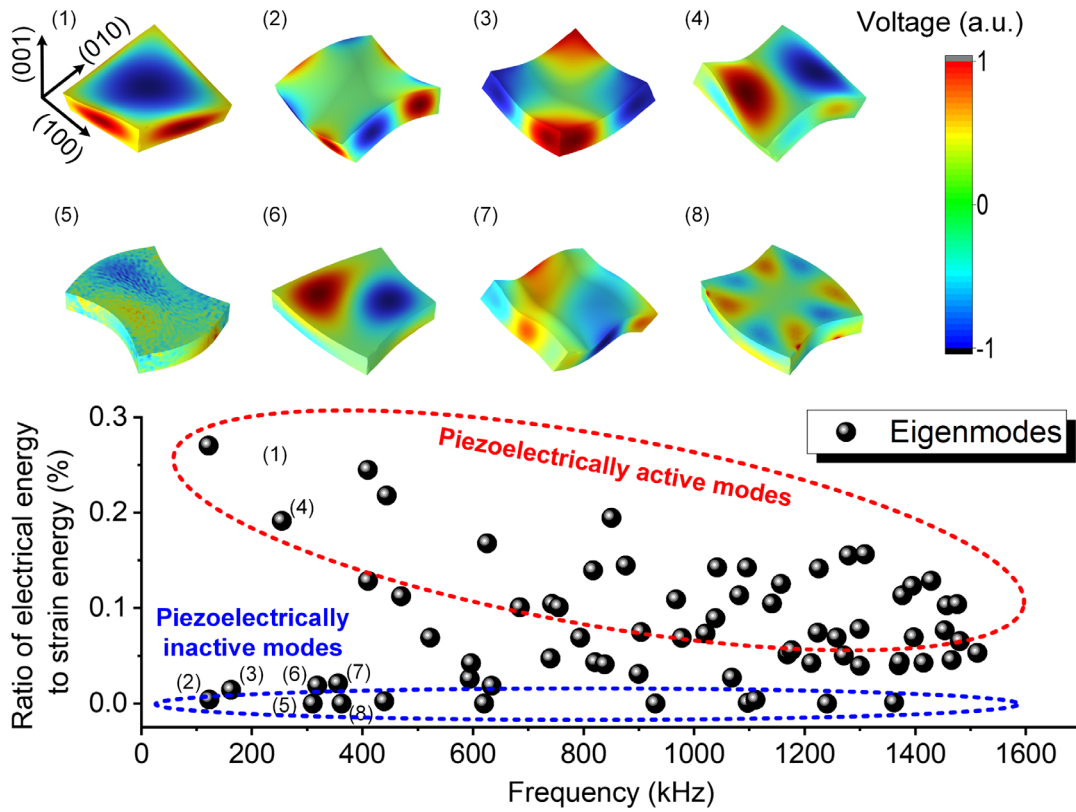
Supplementary Figure 2.1. Schematic of light-induced mechanical absorption spectroscopy (LIMAS).

Figure 2.1 illustrates the setup of light-induced mechanical absorption spectroscopy (LIMAS). The system utilizes resonant ultrasound spectroscopy^{1, 2} (RUS 008, Alamo Creek Engineering) to measure damping (Q^{-1}) and resonance frequency changes (Δf_r). The semiconductor sample is clamped between two opposite corners of two PZT transducers, which are mounted on a vibration

Supplementary Information

isolation stage to minimize external disturbances. The transmitting PZT transducer generates elastic waves with a constant amplitude across a frequency range from kHz to MHz. The receiving PZT transducer detects a large peak in the amplitude-frequency curve when the excitation frequency matched one of the sample's eigenfrequencies (Supplementary Note 3). The Q^{-1} value is derived from the half-bandwidth (-3 dB) of the peak, while f_r is determined from the peak position (Supplementary Note 7). For illumination, various LEDs with emission wavelengths ranging from 320 nm to 1000 nm are used. These LEDs were calibrated using a spectrofluorometer (Horiba, FluoroMax Plus), and their corresponding emission spectra are presented below. The photon flux is measured using a Si-based photodiode power sensor (S120VC, 200 nm-1100 nm, Thorlabs) with a resolution of 1 nW. During the test, the photodiode power sensor is placed near the sample, while the LED is positioned along the central axis shared by both the sensor and the sample, at a sufficient distance from them, ensuring that the measured photon flux accurately represents the actual photon flux incident on the sample. A LabVIEW program is employed to control all the components of the setup. Experiments were conducted under both steady-state conditions (monochromatic and bichromatic light) and transient conditions (with a time resolution of 1 s in this work).

Supplementary Note 3. Piezoelectrically active/inactive eigenmodes



Supplementary Figure 3.1. Piezoelectrically active and inactive eigenmodes of a $5 \times 5 \times 1$ mm ZnS wafer.

Figure 3.1 illustrates the finite element method (FEM) calculated first eight eigenmodes of a $5 \times 5 \times 1$ mm ZnS wafer, along with the first ninety ratios of electrical energy to strain energy. A "piezoelectrically inactive eigenmode" is defined when the ratio approaches zero (blue circle), whereas a "piezoelectrically active eigenmode" corresponds to a nonzero ratio (red circle). For the first eight eigenmodes, (1) and (4) belong to the "piezoelectrically active eigenmode", while (5) and (8) belong to the "piezoelectrically inactive eigenmode". In LIMAS, only piezoelectrically active eigenmodes should be used to analyze carrier recombination processes to ensure a high signal-to-noise ratio (SNR) during testing.

The parameters of ZnS used for FEM calculation here are as follows: mass density 4088 kg/m^3 , elastic coefficients $c_{11}=c_{22}=c_{33}=104.6 \text{ GPa}$, $c_{12}=c_{13}=c_{23}=65.3 \text{ GPa}$, $c_{44}=c_{55}=c_{66}=46.13 \text{ GPa}$.

Supplementary Information

Piezoelectric coefficients $e_{14}=e_{24}=e_{36}=0.14 \text{ C/m}^2$. Relative dielectric coefficients $\varepsilon_{11} = \varepsilon_{22} = \varepsilon_{33} = 8.3$.

Supplementary Note 4. Derivation of Eq. (1)

For compound semiconductors, the constitutive law is³:

$$\begin{cases} T = cS - eE \\ D = eS + \varepsilon E \end{cases} \quad (\text{S1})$$

where T, S are stress and strain; D, E are electric displacement and electric field. c, e , and ε are the elastic, piezoelectric and dielectric constants, respectively. When a uniformly illuminated sample undergoes mechanical vibration, an internal alternating electric field (E) is generated, driving carriers to move and redistributing electrons in localized states (Fig. 1c). Under this circumstance, $n = n_0 + \Delta n + \Delta n'$, $p = p_0 + \Delta p + \Delta p'$, $\Delta p' = -\eta \Delta n'$, $\nabla \cdot D = -qn_{net}$. It is reasonable to assume that the ratio of $\Delta p'$ to $\Delta n'$ is a constant, $\eta \in (0, \infty)$, depending on the specific material and doping conditions. n_{net} denotes net space charge concentration. $fn_{net} = (\Delta n' - \Delta p')$, which means a fraction f of the net space charge is caused by mobile carriers, and the left is due to the redistribution of electrons in localized states (Fig. 1c). Considering the 1D problem, the vibration, continuity, and transport equations can be written as:

$$\begin{cases} \frac{\partial T}{\partial x} = \rho \frac{\partial^2 u}{\partial t^2} \\ \frac{\partial(\Delta n + \Delta n')}{\partial t} = \frac{1}{q} \frac{\partial J_n}{\partial x} - \frac{\Delta n + \Delta n'}{\tau_n} + g, & \frac{\partial(\Delta p + \Delta p')}{\partial t} = -\frac{1}{q} \frac{\partial J_p}{\partial x} - \frac{\Delta p + \Delta p'}{\tau_p} + g \\ J_n = qE\mu_n n + qD_n \frac{\partial \Delta n'}{\partial x}, & J_p = qE\mu_p p - qD_p \frac{\partial \Delta p'}{\partial x} \end{cases} \quad (\text{S2})$$

where u, ρ are displacement and mass density. J_n, J_p are current in the conduction and valence band. τ_n, τ_p are lifetimes of electrons and holes. $g = \alpha\beta\Phi$ is the photogeneration rate, where α is the absorption coefficient, β is quantum yield (carrier pairs generated by each photon), Φ is the photon flux. μ_n, μ_p, D_n, D_p are mobility and diffusion coefficients of electrons and holes. During test, the mechanical vibration amplitude in the sample is negligibly small, ensuring no impact on carrier generation or recombination, so $\frac{d\Delta n}{dt} = -\frac{\Delta n}{\tau_n} + g$, $\frac{d\Delta p}{dt} = -\frac{\Delta p}{\tau_p} + g$, and

Supplementary Information

$$\frac{\partial(\Delta n' - \Delta p')}{\partial t} = \frac{1}{q} \frac{\partial(J_n + J_p)}{\partial x} + \frac{\Delta p'}{\tau_p} - \frac{\Delta n'}{\tau_n} \quad (S3)$$

where $\frac{1}{q} \frac{\partial(J_n + J_p)}{\partial x} = \frac{\partial E}{\partial x} (\mu_n n + \mu_p p) + E \mu_n \frac{\partial \Delta n'}{\partial x} + E \mu_p \frac{\partial \Delta p'}{\partial x} + D_n \frac{\partial^2 \Delta n'}{\partial x^2} - D_p \frac{\partial^2 \Delta p'}{\partial x^2}$, $\Delta p' = -\eta \Delta n'$, and $(\Delta n' - \Delta p') = -\frac{f}{q} \nabla \cdot D$. For small signals, the product of the differentials of D and E is negligible, so

$$\frac{\partial^2 D}{\partial x \partial t} = -\frac{\sigma}{f} \frac{\partial E}{\partial x} + D_{eq} \frac{\partial^3 D}{\partial x^3} - \frac{1}{\tau_{eq}} \frac{\partial D}{\partial x} \quad (S4)$$

Where $\sigma = q[\mu_n(n_0 + \Delta n) + \mu_p(p_0 + \Delta p)]$ is the conductivity, $D_{eq} = (D_n + \eta D_p)/(1 + \eta)$ is the equivalent diffusion coefficient, $\tau_{eq} = (1 + \eta)/\left(\frac{\eta}{\tau_p} + \frac{1}{\tau_n}\right)$ is the equivalent lifetime. As η approaches 0, conduction band electrons dominate, leading to $D_{eq} = D_n$ and $\tau_{eq} = \tau_n$. Conversely, as η approaches ∞ , valence band holes dominate, resulting in $D_{eq} = D_p$ and $\tau_{eq} = \tau_p$.

Assume the time and space dependencies of the plane elastic wave as: $D = D_0 e^{i(kx - \omega t)}$, $E = E_0 e^{i(kx - \omega t)}$. Where $k = \omega/v_0$ is the wave number, $v_0 = \sqrt{c/\rho}$ is the wave velocity, ω is circular frequency of the mechanical vibration, which is typically 10^5 - 10^7 rad/s in our tests. By first solving Eq. (S4) and then substituting the obtained D - E relationship into Eq. (S1), we can determine the mechanical damping (Q^{-1}) and resonance frequency change ($\Delta f_r/f_r$):

$$\left\{ \begin{aligned} Q^{-1} &= \frac{e^2}{c\epsilon} \frac{\omega_c / \omega}{1 + (\omega_c / \omega + \omega / \omega_D + \omega_\tau / \omega)^2} \\ \frac{\Delta f_r}{f_r} &= -\frac{e^2}{2c\epsilon} \left[1 - \frac{1 + (\omega / \omega_D + \omega_\tau / \omega)(\omega / \omega_D + \omega_\tau / \omega + \omega_c / \omega)}{1 + (\omega_c / \omega + \omega / \omega_D + \omega_\tau / \omega)^2} \right] \end{aligned} \right. \quad (S5)$$

Where $\omega_c = \sigma/(f\epsilon)$ is the conductivity frequency, $\omega_D = v_0^2/D_{eq}$ is the diffusion frequency, $\omega_\tau = 1/\tau_{eq}$ is the lifetime frequency. The response of Q^{-1} and $\Delta f_r/f_r$ to illumination can vary depending on the semiconductor type and test conditions. Below, we discuss two possible scenarios:

Case I: Strong n -type or p -type compound semiconductors at room temperature

For strong n -type semiconductors at room temperature (the case for p -type is similar), impurity

Supplementary Information

ionization is significant, resulting in a high electron concentration in the conduction band (n_0) compared to the hole concentration in the valence band (p_0). Consequently, the perturbation of electrons induced by mechanical vibration is much larger than that of holes, leading to $\eta \approx 0$. The corresponding parameters are: $\sigma = q\mu_n(n_0 + \Delta n)$, $\omega_D = v_0^2/D_n$, $\omega_\tau = 1/\tau_n$. If there is no illumination, then $\Delta n = 0$. Table 4.1 lists the ω_c , ω_D , and ω_τ values for several commercial strong n -type and p -type semiconductors under darkness. For direct bandgap n -type or p -type semiconductors, carrier lifetime is estimated based on direct recombination, thus $\omega_\tau \approx c_D n_0$, where $c_D = 10^{-9} \text{cm}^3/\text{s}$ is the estimated direct recombination coefficient. μ_n , D_n and μ_p , D_p follow the Einstein relation.

Table 4.1 Parameters of some commercial n/p -type semiconductors at room temperature⁴

Semi conductor	Conduct ivity type	n_0/p_0 (cm^{-3})	μ_n/μ_p ($\text{cm}^2/\text{V/s}$)	σ ($\text{ohm}^{-1}\text{cm}^{-1}$)	ϵ_r	ω_c (rad/s)	v_0^2 (cm^2/s^2)	D_n/D_p (cm^2/s)	ω_D (rad/s)	ω_τ (rad/s)
GaAs-Zn	p -type	2E19	70	224	13.1	1.9E14	2.2E11	1.8	1.2E11	2E10
GaAs-Te	n -type	5E17	3500	280	13.1	2.4e14	2.2E11	91	2.4E9	5E8
GaP	n -type	4E16	470	3	11.4	3.0E12	3.6E11	12.2	3E10	/
GaP-S	n -type	7E17	270	30	11.4	3e13	3.6E11	7	5E10	/
GaSb	p -type	1.5E17	700	17	16.8	1.1E13	1E11	18.2	5.5E9	1.5E8
GaSb-Zn	p -type	3E18	400	192	16.8	1.3E14	1E11	10.4	9.6E9	3E9
InAs	n -type	3E16	2E4	96	12.3	8.8E13	1.6E11	520	3E8	3E7
InAs-Zn	p -type	5E18	130	104	12.3	9.5E13	1.6E11	3.4	4.7E10	5E9
InP	n -type	8E15	4000	5	9.6	6E12	1.2E11	104	1.1E9	8E6
InP-Zn	p -type	1E18	3000	480	9.6	5.6E14	1.2E11	78	1.5E9	1E9
InSb-Te	n -type	5E17	12500	1000	17.7	6.4E14	1.1E11	325	3.4E8	5E8
InSb-Ge	n -type	5E16	250	2	17.7	1.3E12	1.1E11	6.5	1.7E10	5E7

According to Table 4.1, $\omega, \omega_\tau \ll \omega_D \ll \omega_c$, resulting in Q^{-1} in Eq. (S5) being zero, while $\Delta f_r/f_r$ remains constant. Q^{-1} and $\Delta f_r/f_r$ have no response to illumination in this condition.

Supplementary Information

Case II: Compound semi-insulators at room temperature

In this case, impurity ionization is weak, so both conduction band electrons and valence band holes contribute to conductivity, i.e., $\sigma = q[\mu_n(n_0 + \Delta n) + \mu_p(p_0 + \Delta p)]$. If there is no illumination, $\Delta n, \Delta p = 0$. Table 4.2 lists the values of ω_c , ω_D , and ω_τ for several commercial semi-insulators at room temperature under darkness.

Table 4.2 Parameters of some commercial semi-insulators at room temperature⁴

Semi-insulator	Conductivity type	n_0/p_0 (cm^{-3})	μ_n/μ_p (cm^2/Vs)	σ ($ohm^{-1}cm^{-1}$)	ϵ_r	ω_c (rad/s)	v_0^2 (cm^2/s^2)	D_n/D_p (s)	ω_D (rad/s)	ω_τ (rad/s)
GaAs	S-I	/	5500	1E-8	13.1	8.6E3	2.2E11	143	1.5E9	1E-2
GaP	S-I	9E8	150	1E-8	11.4	1E4	3.6E11	3.9	9.2E10	4E-1
InP	S-I	/	2500	2E-8	9.6	2.3E4	1.2E11	65	1.9E9	5E-2
InGaAs-Fe	S-I	/	1500	5E-8	13.9	4E4	1E11	40	2.6E9	2E-1
CdS	S-I	/	350	1E-10	6	188	3.4E11	9.1	3.7E10	1.8E-3
CdSe	S-I	/	1100	1E-11	6.5	17	9E10	28.6	3.2E9	5.7E-5
CdTe	S-I	/	1050	1E-11	9.0	12	9E10	27.3	3.3E9	6E-5
ZnSe	S-I	/	500	1E-8	6.6	1.7E4	1.2E11	13	9.2E9	1.2E-1
ZnTe	S-I	/	340	1E-8	9.6	1.1E4	9E10	8.84	1E10	1.8E-1
ZnS	S-I	/	500	1E-10	10	113	1.6E11	13	1.2E10	1.3E-3

According to Table 4.2, in the dark, $\omega_\tau \ll \omega_c < \omega \ll \omega_D$, so

$$\begin{cases} Q^{-1} = \frac{e^2}{c\epsilon} \frac{\omega_c / \omega}{1 + (\omega_c / \omega)^2} \\ \frac{\Delta f_r}{f_r} = -\frac{e^2}{2c\epsilon} \frac{(\omega_c / \omega)^2}{1 + (\omega_c / \omega)^2} \end{cases} \quad (S6)$$

For steady-state illumination, $\Delta n \gg n_0$, $\Delta p \gg p_0$, $\omega_c = q(\mu_n \Delta n + \mu_p \Delta p) / (f\epsilon)$. When $\omega_c < \omega$,

Supplementary Information

Q^{-1} increases with photo flux Φ , when $\omega_c = \omega$, Q^{-1} reaches its maximum, and when $\omega_c > \omega$, Q^{-1} decreases as photo flux increases. During illumination switching on/off, Δn and Δp become time-dependent, leading to time-dependent behavior in Q^{-1} and $\Delta f_r/f_r$.

In this study, the ZnS single crystal samples fall under the second scenario, so Eq. (S6) is used.

Supplementary Note 5. γ value, damping, and resonance frequency change for each individual recombination pathway

According to Eq. (S6), Q^{-1} and $\Delta f_r/f_r$ depend on ω_c . $\omega_c = q(\mu_n \Delta n + \mu_p \Delta p)/(f\varepsilon)$, where Δn and Δp are functions of photo flux Φ for steady-state conditions or function of time t for transient state conditions, determined by the overall recombination kinetics. Since the mechanical vibration amplitude is negligibly small, the carrier generation and recombination processes can still be described as:

$$\begin{cases} \frac{d\Delta n}{dt} = -\frac{\Delta n}{\tau_n} + g \\ \frac{d\Delta p}{dt} = -\frac{\Delta p}{\tau_p} + g \end{cases} \quad (\text{S7})$$

Below, we consider different individual recombination pathways.

Direct recombination

Considering direct recombination in semi-insulators (see process (i) in Fig. 1d):

$$r_{direct} = c_D (n_0 \Delta p + p_0 \Delta n + \Delta n \Delta p) \quad (\text{S8})$$

where c_D is direct recombination coefficient. Assuming no traps, or that Δn and Δp are significantly larger than the trap concentration, we obtain $\Delta n = \Delta p$, $\frac{\Delta n}{\tau_n} = \frac{\Delta p}{\tau_p} = c_D \Delta n \Delta p$

($\Delta n, \Delta p \gg n_0, p_0$). For steady-state illumination, $\frac{\Delta n}{\tau_n} = c_D (\Delta n)^2 = g = \alpha\beta\Phi$, $\omega_c = \frac{q(\mu_n + \mu_p)}{(f\varepsilon)} (\alpha\beta/$

Supplementary Information

$c_D)^{1/2}\Phi^{1/2}$, so $\gamma = 2$. For switch-off processes, $\frac{d\Delta n}{dt} = -c_D(\Delta n)^2$, $\Delta n = \frac{1}{c_D t + 1/\Delta n_0}$, where Δn_0 represents the initial photo-generated electron concentration. For switch-on, $\frac{d\Delta n}{dt} = -c_D(\Delta n)^2 + g$, $\Delta n = \Delta n_\infty \tanh(\sqrt{\Delta n_\infty^2 c_D^2 t})$, where $\Delta n_\infty = (g/c_D)^{1/2}$ represents the final photo-generated electron concentration.

Trap-assisted recombination (Shockley-Read-Hall recombination)

Trap-assisted recombination, also known as Shockley-Read-Hall⁵ (SRH) recombination, via a defect level in the bandgap (see process (ii) in Fig. 1d):

$$r_{trap} = \frac{c_n c_p (n_0 \Delta p + p_0 \Delta n + \Delta n \Delta p)}{c_n (n_0 + n_1 + \Delta n) + c_p (p_0 + p_1 + \Delta p)} N_r = \frac{c_n c_p N_r}{c_n + c_p} \Delta n \quad (S9)$$

where N_r is the trap density (concentration of recombination center), c_n and c_p are electron and hole capture coefficients of this recombination center. n_1 and p_1 are the concentration of conduction band electrons and valence band holes, respectively, when the Fermi level is equal to the defect energy level. Here, assuming N_r is very small or under strong photogeneration ($N_r \ll \Delta n, \Delta p$), we obtain $\Delta n = \Delta p$, $\frac{\Delta n}{\tau_n} = \frac{\Delta p}{\tau_p} = \frac{c_n c_p N_r}{c_n + c_p} \Delta n = \frac{\Delta n}{\tau_T} = c_T \Delta n$, where τ_T is the lifetime for trap-assisted recombination. For steady-state, $\omega_c = \frac{q(\mu_n + \mu_p)}{(f\varepsilon)} \alpha \beta \tau_T \Phi$, $\gamma = 1$. For switch-off, $\Delta n = \Delta n_0 e^{-t/\tau_T}$. For switch-on, $\Delta n = \Delta n_\infty (1 - e^{-t/\tau_T})$, $\Delta n_\infty = g \tau_T$.

Auger recombination

$$r_{Auger} = c_A (n^3 - n_0^3) = c_A \Delta n^3 \quad (S10)$$

For Auger recombination⁶ (see process (iii) in Fig. 1d), $\frac{\Delta n}{\tau_n} = \frac{\Delta p}{\tau_p} = c_A (\Delta n)^3$, where c_A is the Auger recombination coefficient. Here, we still assume $\Delta n = \Delta p$. For steady-state, $\omega_c = \frac{q(\mu_n + \mu_p)}{(f\varepsilon)} (\alpha \beta / c_A)^{1/3} \Phi^{1/3}$, $\gamma = 3$. For switch-off, $\Delta n = \frac{1}{\sqrt{2c_A t + 1/(\Delta n_0)^2}}$.

Supplementary Information

Auger recombination can be ignored in high-purity ZnS single crystals due to their large bandgap and low carrier concentrations.

Sublinear recombination

$$r_{\text{sublinear}} = c_{\gamma} \Delta n^{\gamma}, \quad \gamma \in (0,1) \quad (\text{S11})$$

Sublinear recombination^{7, 8} is more complex than trap-assisted recombination, as it involves multiple saturated defect levels (see process (iv) in Fig. 1d). Due to the saturation of these defect levels, the recombination rate is not proportional to the carrier concentration, resulting in a recombination exponent $\gamma < 1$. In general case, $\frac{\Delta n}{\tau_n} = \frac{\Delta p}{\tau_p} = c_{\gamma} (\Delta n)^{\gamma}$, $\gamma=3, 2$, and 1 represent the above-mentioned Auger, direct, and trap-assisted recombination, respectively. When $\gamma < 1$, representing the sublinear recombination. For steady-state sublinear recombination, $\omega_c = \frac{q(\mu_n + \mu_p)}{(f\varepsilon)} (\alpha\beta/c_{\gamma})^{1/\gamma} \Phi^{1/\gamma}$. For switch-off, $\Delta n = (1 - \gamma)^{\frac{1}{1-\gamma}} \left[\frac{1}{1-\gamma} (\Delta n_0)^{1-\gamma} - c_{\gamma} t \right]^{\frac{1}{1-\gamma}}$.

Other recombination

Other types of recombination, such as surface recombination (primarily occurs at the surface or interface), exciton recombination (primarily occurs in quantum dots), and band-tail recombination (primarily occurs in amorphous), are not considered in this high-purity bulk ZnS single crystal here.

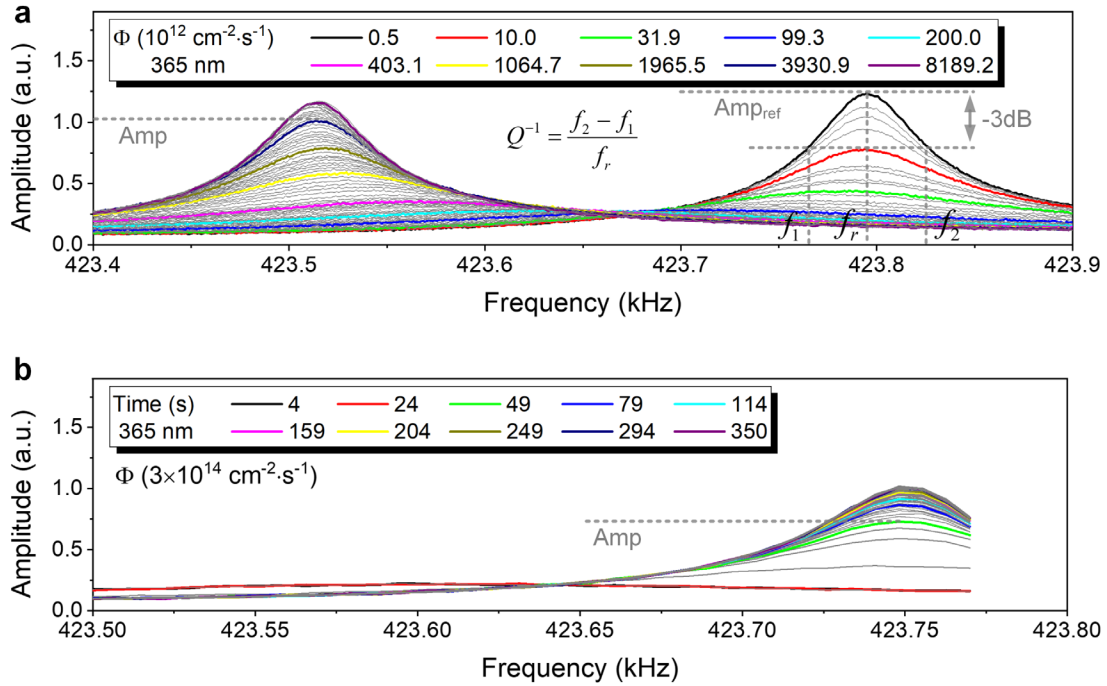
Supplementary Note 6. Parameters used to calculate Fig. 1e

For calculation of Fig. 1e, the mechanical vibration circular frequency ω is set as $2.6 \times 10^6 \text{ rad/s}$, elementary charge $q = 1.6 \times 10^{-19} \text{ C}$, $\mu_n + \mu_p = 500 \text{ cm}^2/\text{V/s}$, $\varepsilon = \varepsilon_r \varepsilon_0 = 8.854 \times 10^{-13} \text{ F/cm}$, $f = 1$, absorption coefficient $\alpha = 0.001 \text{ cm}^{-1}$, quantum yield $\beta = 0.1$. For steady-state illumination, photon flux Φ is from $10^3 \text{ cm}^{-2}/\text{s}$ to $10^{20} \text{ cm}^{-2}/\text{s}$. The direct recombination coefficients⁹ c_D is assumed to be $10^{-9} \text{ cm}^3/\text{s}$. For trap-assisted recombination⁷,

Supplementary Information

$c_n = c_p$ is assumed to be $10^{-8} \text{ cm}^3/\text{s}$, N_r is assumed to be 10^7 cm^{-3} , so $\tau_T = 20\text{s}$. For Auger recombination⁶, c_A is assumed to be $10^{-27} \text{ cm}^6/\text{s}$. For sublinear recombination, γ is set as $1/2$, $c_{0.5}$ is assumed to be $10^9 \text{ cm}^{-3/2}/\text{s}$.

Supplementary Note 7. Extract damping and resonance frequency from the measured amplitude-frequency curve



Supplementary Figure 7.1 Extract damping and resonance frequency from the measured amplitude-frequency curves under steady-state and transient illuminations. **a** Measured amplitude-frequency curves for ZnS (i) under steady-state 365 nm monochromatic light at various photon flux Φ . **b** Time-dependent amplitude-frequency curves for ZnS (i) upon switching off 365 nm monochromatic light (with initial photon flux $\Phi = 3 \times 10^{14} \text{ cm}^{-2} \cdot \text{s}^{-1}$).

Figure 7.1a shows the measured amplitude-frequency curves for ZnS (i) under steady-state 365 nm monochromatic light, with photon flux ranging from 10^{12} to $10^{17} \text{ cm}^{-2} \cdot \text{s}^{-1}$. Under darkness, $\Phi = 0.5 \times 10^{12} \text{ cm}^{-2} \cdot \text{s}^{-1}$, the Q^{-1} can be calculated as¹⁰:

Supplementary Information

$$Q^{-1} = \frac{f_2 - f_1}{f_r} \quad (\text{S12})$$

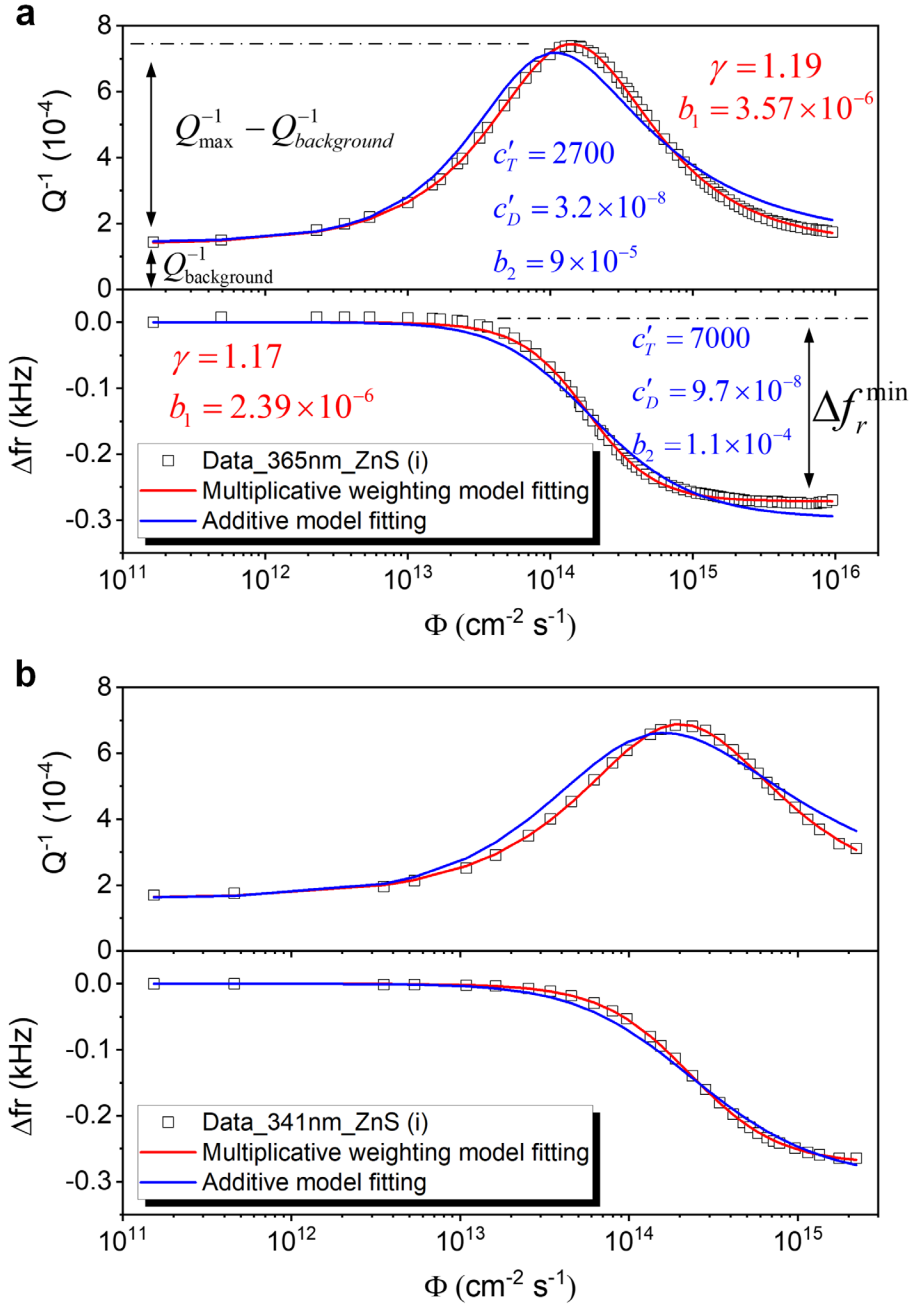
where f_2 and f_1 is derived from the half-bandwidth (-3 dB) of the peak, f_r is determined from the peak position (Figure 7.1a).

For convenient, the Q^{-1} under other illumination conditions can be calculated as¹⁰:

$$Q^{-1} = Q_{ref}^{-1} \frac{Amp_{ref}}{Amp} \quad (\text{S13})$$

where Q_{ref}^{-1} and Amp_{ref} represent the damping and maximum value of the reference amplitude-frequency curves (i.e., the curve measured in darkness). While Q^{-1} and Amp denote the damping and maximum value of the amplitude-frequency curves measured under other illumination conditions. As shown in Figure 7.1a, with increasing photon flux, Amp first decreases and then increases, indicating Q^{-1} initially rises and subsequently falls, forming a peak in the Φ - Q^{-1} plot. Meanwhile, f_r exhibits a sigmoidal transition from the unrelaxed to the relaxed state. Figure 7.1b shows that Q^{-1} gradually recovers after the light is switched off.

Supplementary Note 8. Fit the photon flux-damping and photon flux-resonance frequency change curve of ZnS using two models



Supplementary Figure 8.1. Using the multiplicative weighting model and the conventional additive model to fit the steady-state Φ - Q^{-1} and Φ - Δf_r curves of ZnS (i). **a** ZnS (i) under steady-state 365 nm monochromatic light. **b** ZnS (i) under steady-state 341 nm monochromatic light.

Supplementary Information

According to the amplitude-frequency curves measured under steady-state monochromatic light at various photon flux Φ , we can obtain the Φ - Q^{-1} and Φ - Δf_r curves (Supplementary Note 7). Here we use the multiplicative weighting model and the conventional additive model to fit the Φ - Q^{-1} and Φ - Δf_r curves of ZnS, respectively.

For the multiplicative weighting model fitting, $\alpha\beta\Phi \propto (\Delta n)^\gamma$, so $\omega_c \propto \Delta n \propto \Phi^{1/\gamma}$:

$$\begin{cases} Q^{-1} = Q_{background}^{-1} + 2 \times (Q_{max}^{-1} - Q_{background}^{-1}) \frac{\omega_c / \omega}{1 + (\omega_c / \omega)^2} \\ \Delta f_r = \Delta f_r^{min} \frac{(\omega_c / \omega)^2}{1 + (\omega_c / \omega)^2} \\ \omega_c = b_1 \times \Phi^{1/\gamma} \end{cases} \quad (S14)$$

Where $Q_{background}^{-1}$ and Q_{max}^{-1} represent the background and maximum mechanical damping, respectively. For Φ - Q^{-1} fitting, $Q_{background}^{-1}$, Q_{max}^{-1} , b_1 , and γ are the fitting parameters, while for Φ - Δf_r fitting, Δf_r^{min} , b_1 , and γ are the fitting parameters. The extracted b_1 and γ values from the Φ - Q^{-1} and Φ - Δf_r curves are nearly identical (Figure 8.1a), validating both our theoretical framework for LIMAS and the applicability of the multiplicative weighting model to ZnS.

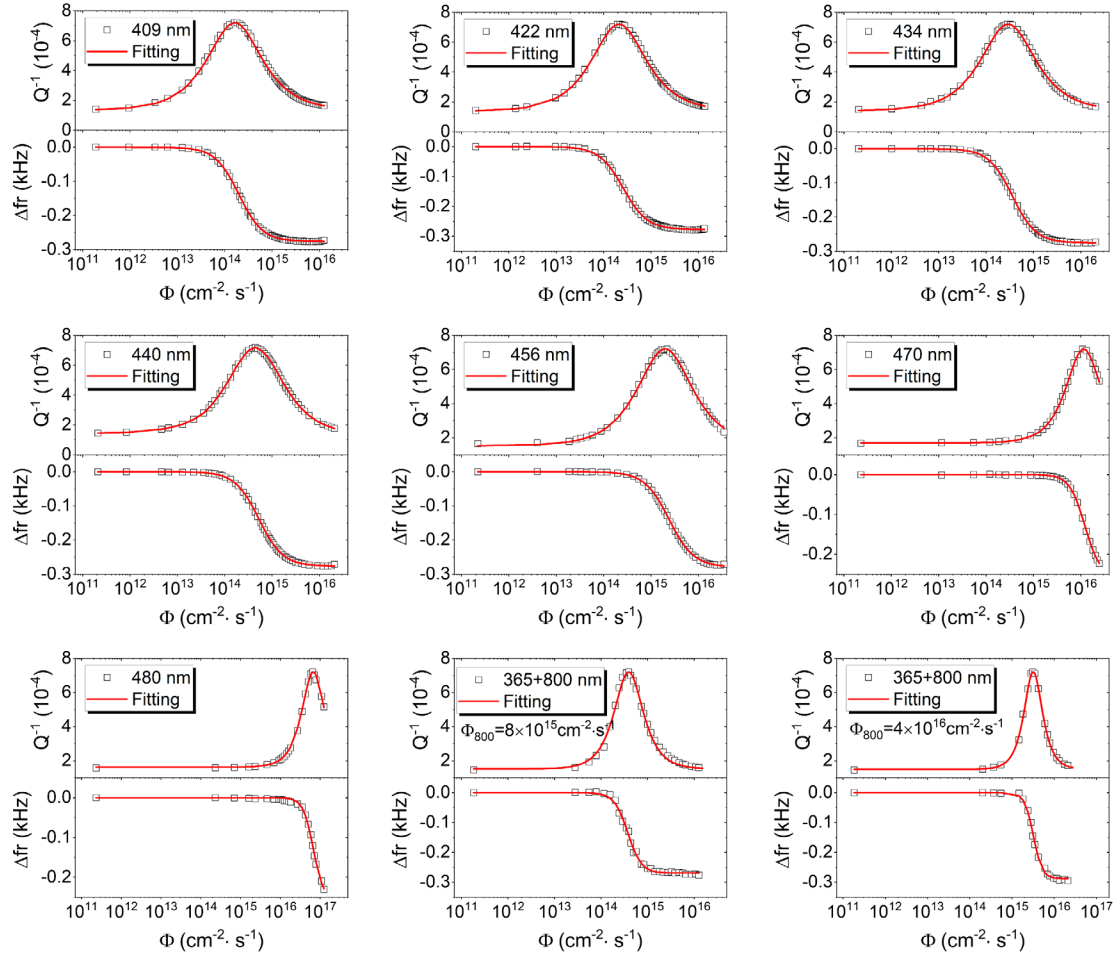
For the additive model fitting under steady-state 365 nm and 341 nm illumination, we consider the trap-assisted and direct recombination: $c_T \Delta n + c_D \Delta n^2 = \alpha\beta\Phi$, i.e., $c'_T \Delta n + c'_D \Delta n^2 = \Phi$

$$\begin{cases} Q^{-1} = Q_{background}^{-1} + 2 \times (Q_{max}^{-1} - Q_{background}^{-1}) \frac{\omega_c / \omega}{1 + (\omega_c / \omega)^2} \\ \Delta f_r = \Delta f_r^{min} \frac{(\omega_c / \omega)^2}{1 + (\omega_c / \omega)^2} \\ \omega_c = b_2 \times \frac{-c'_T + \sqrt{(c'_T)^2 + 4c'_D \Phi}}{2c'_D} \end{cases} \quad (S15)$$

Where c_T , c_D are trap-assisted and direct recombination coefficients, respectively. For Φ - Q^{-1} curve fitting, $Q_{background}^{-1}$, Q_{max}^{-1} , c'_T , c'_D , b_2 are fitting parameters, while for Φ - Δf_r curve fitting, Δf_r^{min} , c'_T , c'_D , b_2 are fitting parameters.

Supplementary Information

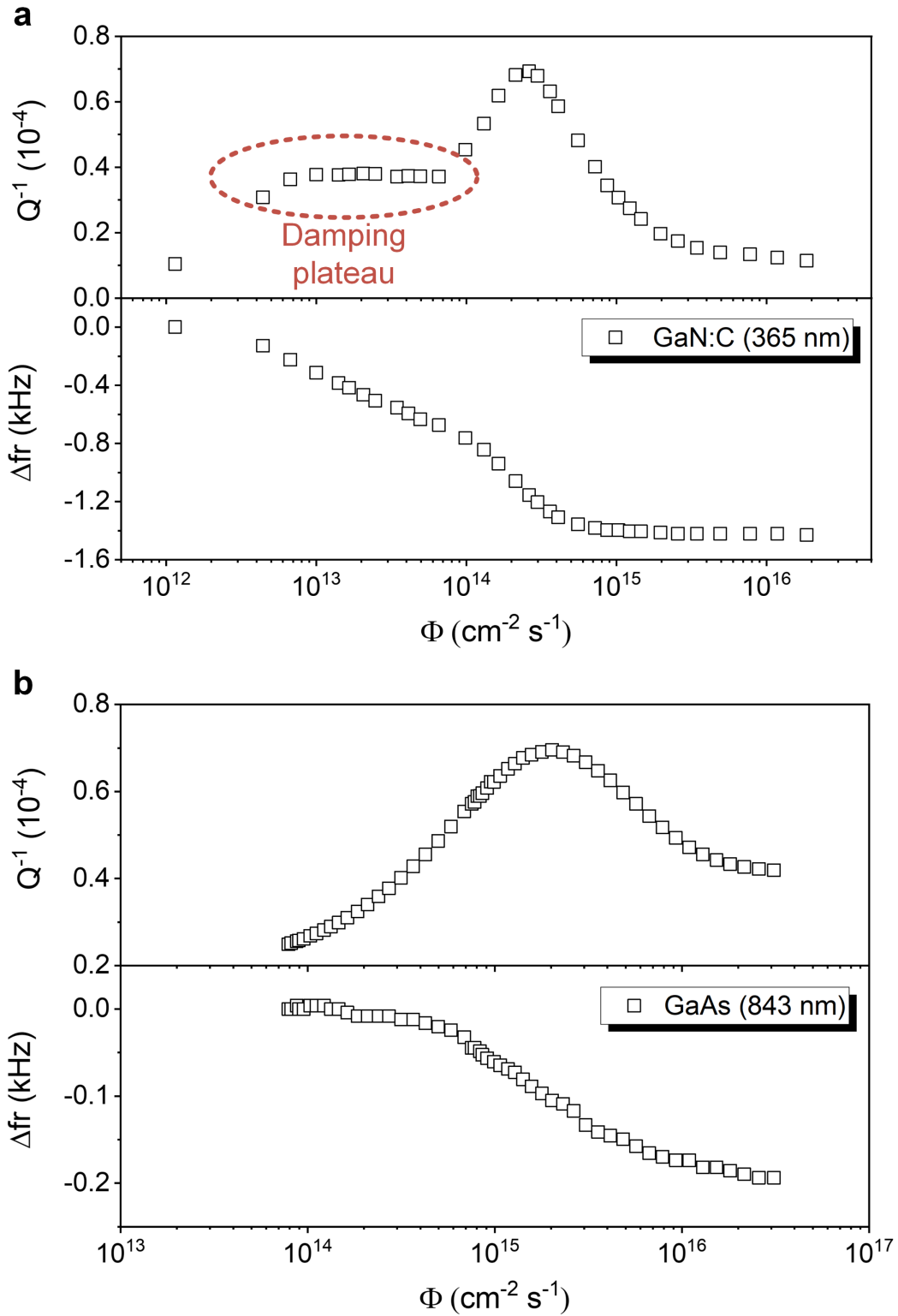
Overall, the multiplicative weighting model provides an excellent fit to the experimental data, as shown by the red curves in Figure 8.1. In contrast, the additive model—despite including an additional fitting parameter—fails to accurately reproduce the data (blue curves in Figure 8.1), due to its inability to account for the coupling and competition between recombination pathways.



Supplementary Figure 8.2. Using the multiplicative weighting model to fit the steady-state $\Phi-Q^{-1}$ and $\Phi-\Delta f_r$ curves of ZnS (i) under different illumination conditions.

Figure 8.2 demonstrates the multiplicative model's robustness by providing consistently accurate fits to ZnS experimental data collected under various illumination conditions.

Supplementary Note 9. Photon flux-damping and photon flux-resonance frequency change curves for GaN:C and GaAs



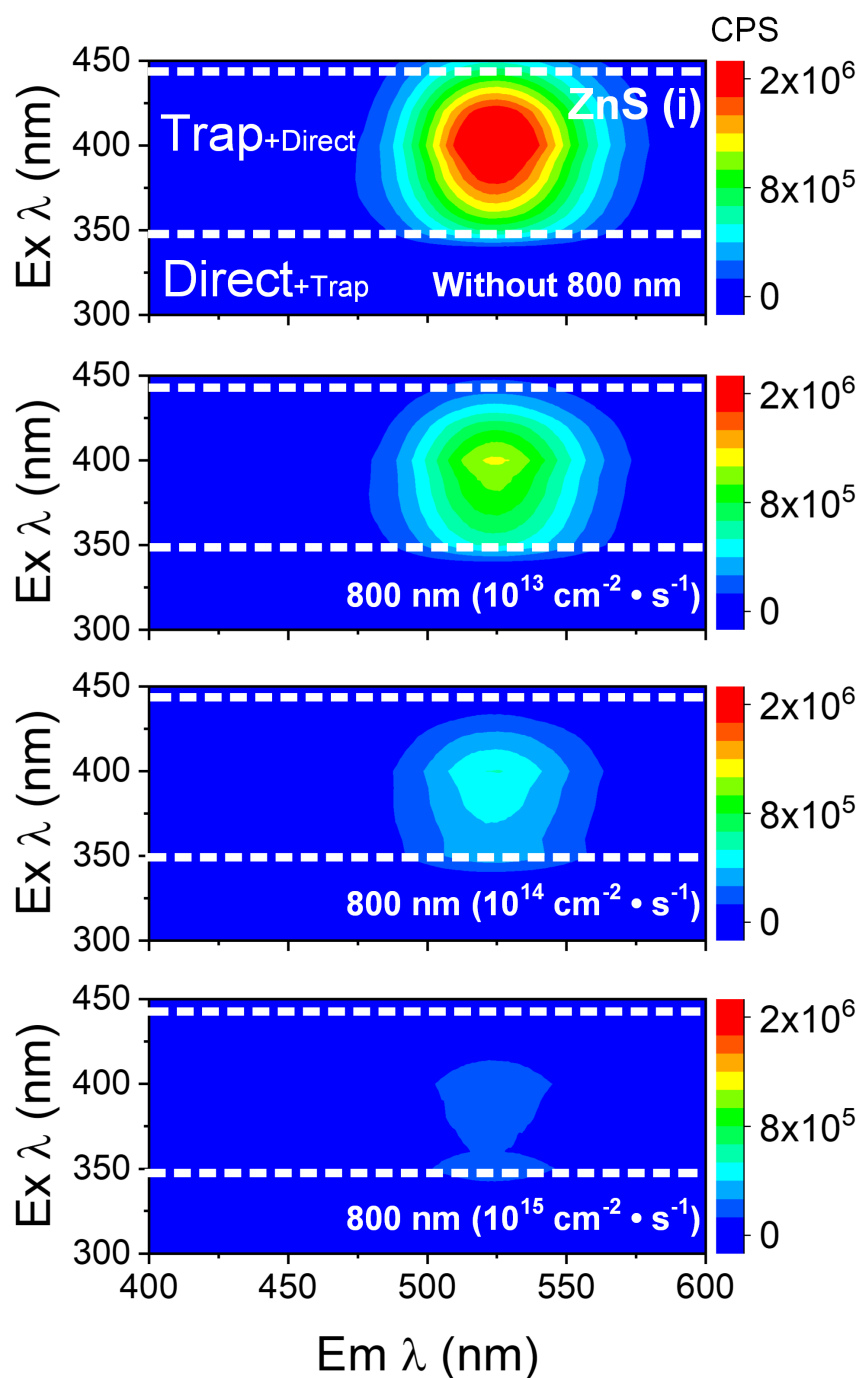
Supplementary Figure 9.1. Steady-state photon flux-damping (Φ - Q^{-1}) and photon flux-resonance

Supplementary Information

frequency change curves ($\Phi-\Delta f_r$) for other semiconductors. **a** GaN:C (carbon doped) under 365 nm monochromic light. **b** GaAs under 843 nm monochromic light.

To further validate LIMAS, we performed tests on the III–V semiconductors GaAs and carbon-doped GaN (GaN:C). Unlike ZnS, these materials do not exhibit ideal anelastic behavior, as evidenced by the absence of a perfect Lorentzian peak in the $\Phi-Q^{-1}$ curves. Instead, GaN:C shows a damping plateau (Figure 9.1a), which may be associated with electron trapping processes. These observations suggest that the multiplicative weighting model for the total recombination rate in ZnS is a special case. According to the literature¹¹, photon-impedance measurements on the II–VI semiconductor CdS also support the multiplicative weighting model. In our view, whether the total recombination rate follows the multiplicative weighting model may depend on the fundamental properties of semiconductors. II-VI semiconductors, with greater ionicity due to larger electronegativity differences, exhibit stronger p-d coupling and larger valence band offsets^{12, 13}. Additionally, their negative piezoelectric coefficients¹⁴, unlike the positive values in III-V semiconductors, influence charge displacement and may explain the validity of the model. To fully elucidate the formation mechanisms of the multiplicative weighting model in ZnS, further investigation is needed. Furthermore, the tests of GaN:C and GaAs also demonstrate that LIMAS is a powerful tool for studying complex electron behaviors (such as trapping and detrapping) in a variety of semiconductors and will be widely used in the near future.

Supplementary Note 10. Photoluminescence quenching contour maps

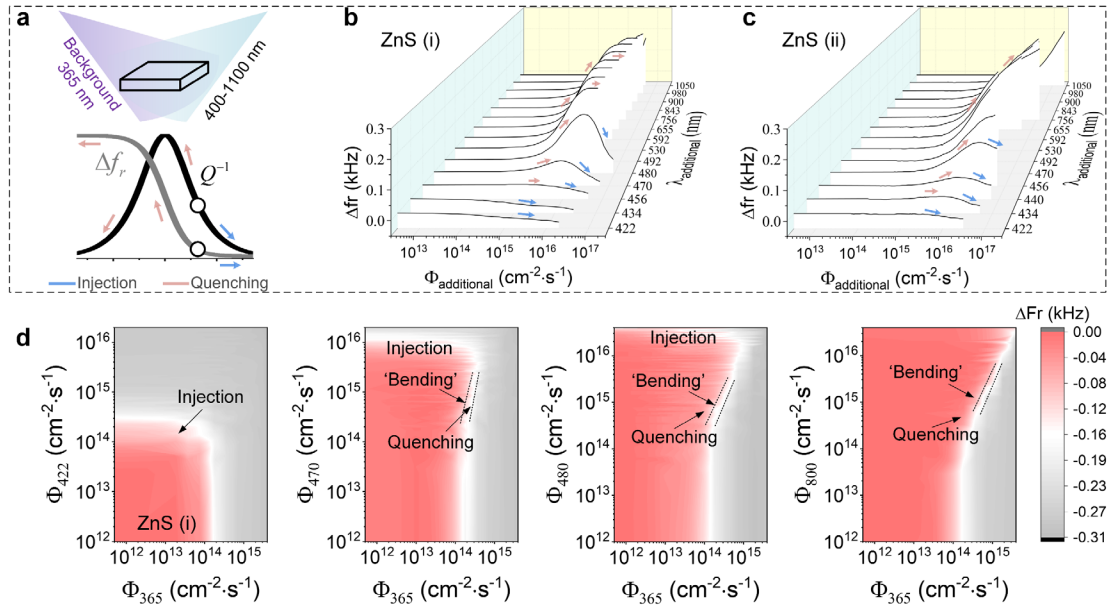


Supplementary Figure 10.1. Photoluminescence quenching contour maps of ZnS (i), measured using a spectrometer with excitation wavelengths ranging from 300 nm to 450 nm and detected emission wavelengths from 400 nm to 600 nm. An additional 800 nm LED with varying photon flux was used to induce quenching effects.

Supplementary Information

Figure 10.1 presents the photoluminescence contour map of ZnS (i), measured using a spectrometer with excitation wavelengths ranging from 300 nm to 450 nm and detected emission wavelengths from 400 nm to 600 nm. An additional 800 nm LED with varying photon flux was used to induce quenching effects. A bandpass filter was employed to eliminate any direct contribution from the 800 nm light. The added 800 nm illumination reduces the intensity of the green emission without shifting its characteristic wavelength, suggesting a suppression of trap-assisted recombination. Based on this observation, the 365 nm UV light is selected as the background excitation in Fig. 3, as it predominantly promotes trap-assisted recombination in ZnS.

Supplementary Note 11. Resonance frequency change in ZnS under steady-state bichromatic illumination

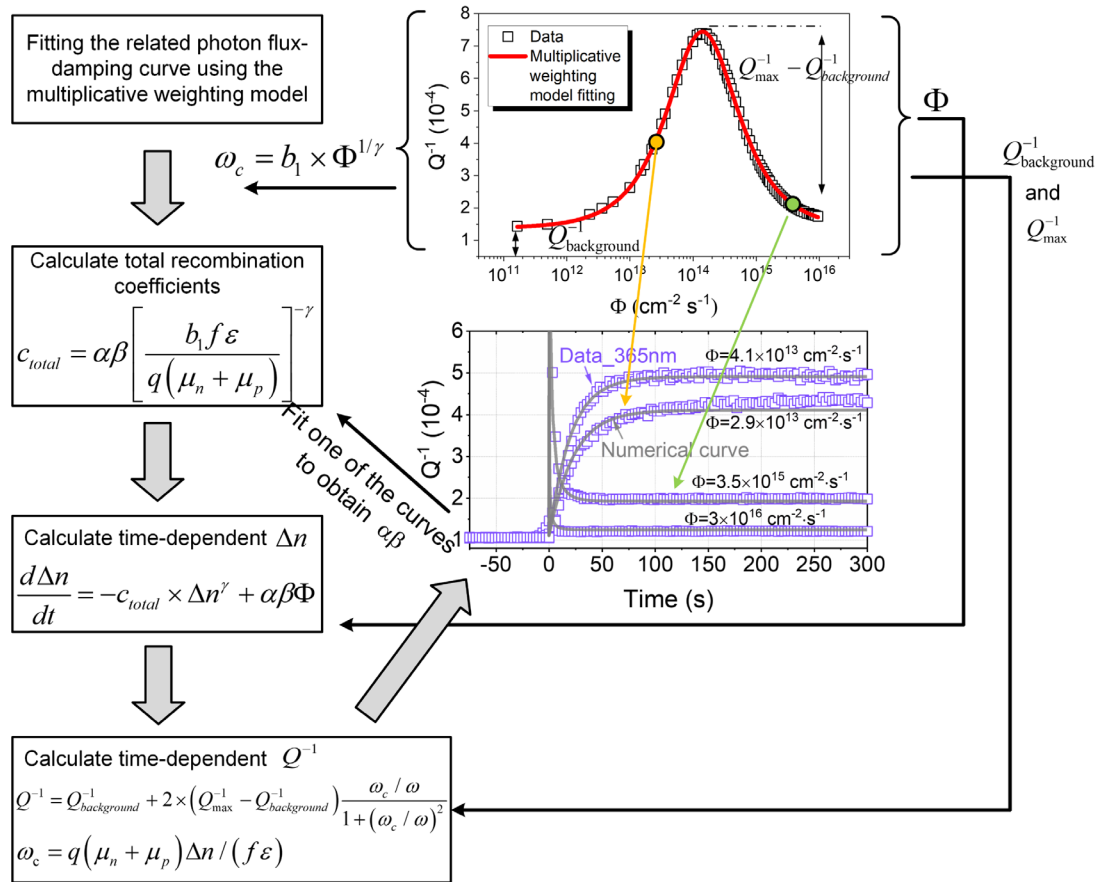


Supplementary Figure 11.1. Resonance frequency change in ZnS under steady-state bichromatic illumination. **a-c** Responses of Δf_r in ZnS samples (i) and (ii) to constant-intensity 365 nm UV light, combined with an additional light source (400 nm-1100 nm) with varying photon flux ($10^{12} \text{ cm}^{-2} \cdot \text{s}^{-1}$ - $10^{17} \text{ cm}^{-2} \cdot \text{s}^{-1}$). **d** Contour maps of Δf_r in ZnS (i) under different bichromatic illumination conditions.

Supplementary Information

Figure 11.1 illustrates the resonance frequency change (Δf_r) in ZnS under steady-state bichromatic illumination. For ZnS (i), 365 nm UV light combined with additional light below 440 nm induces only injection (Figure 11.1b), leading to a decrease in f_r . When the additional light falls between 440 nm and 500 nm, injection and quenching compete, producing peaks in Δf_r curves (Figure 11.1b). Beyond 520 nm, quenching dominates, causing an increase in Δf_r (Figure 11.1b). ZnS (ii) follows similar trends, but quenching occurs at a shorter wavelength (~ 430 nm, Figure 11.1c). Figure 11.1d shows the contour maps of Δf_r in ZnS (i) under different bichromatic illumination conditions. The 'bending' observed in the Δf_r contour maps correspond to the quenching effect.

Supplementary Note 12. Calculate time-dependent damping during the transient process

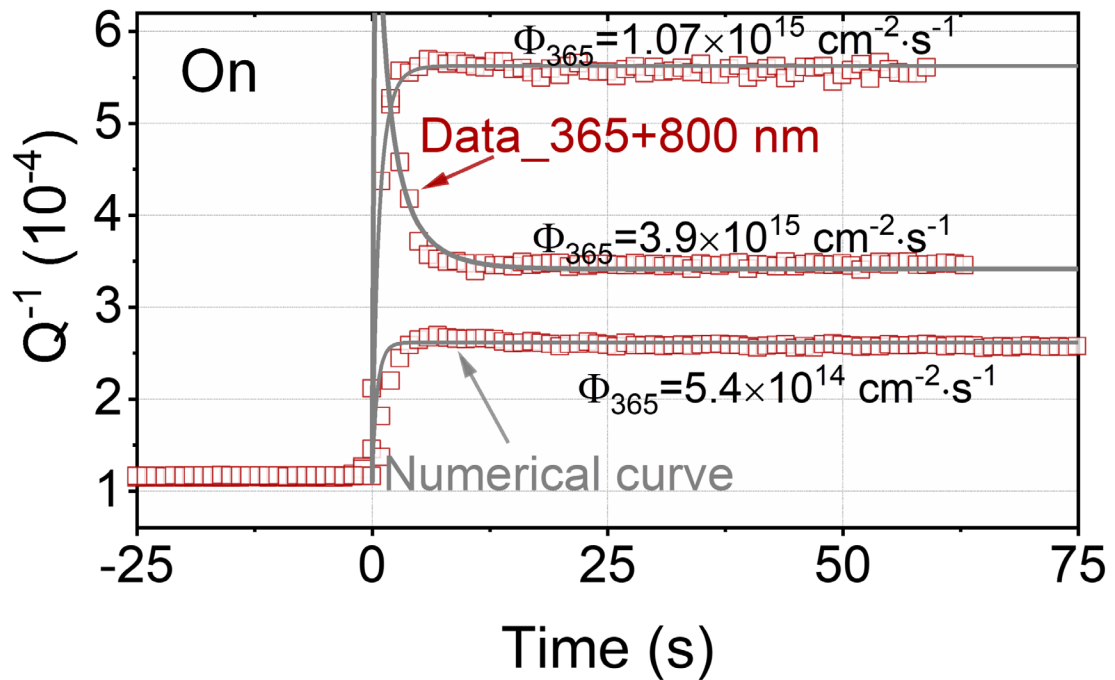


Supplementary Figure 12.1. Flowchart for calculating damping during the transient switch-on

process

Supplementary Information

Figure 12.1 presents a flowchart outlining the numerical procedure for calculating damping during the transient switch-on process. First, the measured photon flux–damping curve under steady-state conditions is fitted using a multiplicative model to extract the parameters b_1 and γ . Next, the parameters q , $\mu_n + \mu_p$, and ε are obtained from the literature, f is set to 1, and $\alpha\beta$ is manually assigned to compute the recombination coefficient c_{total} . Time-dependent damping is then calculated using the rate equation. By fitting the computed curve to the experimentally measured one, an appropriate value for $\alpha\beta$ can be identified. Finally, by varying the photon flux Φ , the time-dependent damping curves under different photon flux can be determined. The procedure for the switch-off case is the same and is not repeated here.



Supplementary Figure 12.2. Measured and numerically calculated (assuming constant w_i) time dependence of Q^{-1} upon switching on of biochromatic light (365 nm + 800 nm, where the 800 nm light maintains open status and only 365 nm light at various photon flux is switched.

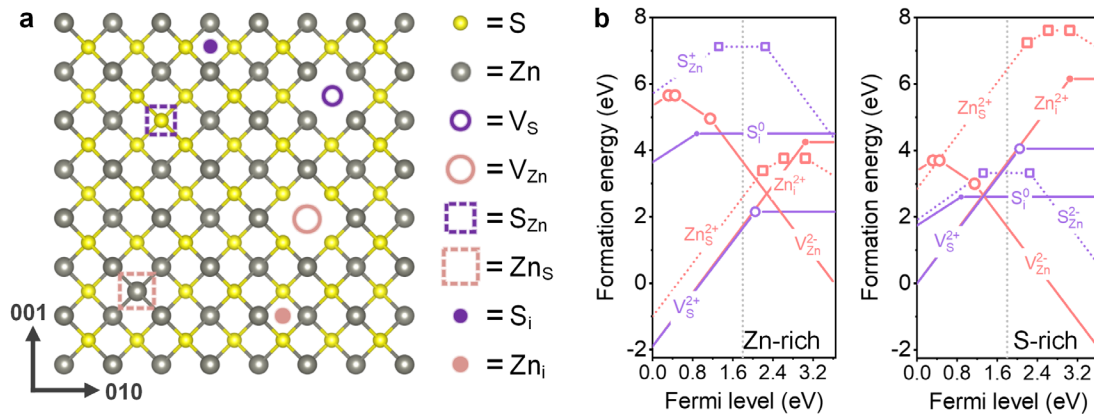
$$\Phi_{800nm} = 10^{15} \text{ cm}^{-2} \cdot \text{s}^{-1}.$$

Figure 12.2 shows a strong agreement between measured and numerically calculated (assuming

Supplementary Information

constant w_i) time dependence of Q^{-1} upon switching on of biochromatic light (365 nm + 800 nm, where the 800 nm light maintains open status and only 365 nm light at various photon flux is switched. $\Phi_{800nm} = 10^{15} \text{ cm}^{-2} \cdot \text{s}^{-1}$), supporting our multiplicative weighting model, reflecting a constant- θ trajectory in Fig. 4e.

Supplementary Note 13. Trap-assisted and sublinear recombination related intrinsic defects



Supplementary Figure 13.1 Intrinsic point defects in ZnS associated with trap-assisted and sublinear recombination. **a** Intrinsic point defects in ZnS: vacancies (V_S , V_{Zn}), interstitials (S_i , Zn_i), and antisites (S_{Zn} , Zn_S). **b** Defect formation energy as a function of Fermi level relative to the valence band maximum.

ZnS contains various intrinsic point defects (Figure 13.1a), including sulfur and zinc vacancies (V_S , V_{Zn}), interstitials (S_i , Zn_i), and antisites (S_{Zn} , Zn_S). These defects act as donors or acceptors, with formation energies dependent on the growth environment¹⁵⁻¹⁷. Fig. 2 and 3 show that trap-assisted recombination in ZnS is linked to a donor defect more prevalent in Zn-rich conditions. This is evidenced by the stronger green photoluminescence in ZnS (i), grown under Zn-rich conditions, compared to ZnS (ii), grown under S-rich conditions. Based on the calculated formation energies in Figure 13.1b, zinc antisite (Zn_S) is identified as the trap-assisted recombination center. With a

Supplementary Information

charge transition point (2+/+ or +/0) near 2.4 eV, it effectively captures conduction band electrons, which then recombine with valence band holes, emitting green light. For sublinear recombination, a defect with a higher concentration than Zn_S must serve as the initial electron reservoir at thermal equilibrium. Figure 13.1b identifies sulfur vacancy (V_S) as the most likely candidate. Its lower formation energy ensures a higher concentration¹⁸, and its charge transition point (2+/0) near the center of the bandgap leads to full electron occupation at thermal equilibrium. Under low-energy monochromatic light (0.66 E_g -0.8 E_g) or with additional high-wavelength light (<0.8 E_g), electrons from V_S are excited and transferred to Zn_S , progressively saturating both defect levels, leading to sublinear recombination, altering the emission properties.

All density functional theory (DFT) calculations are performed using the Vienna Ab initio Simulation Package (VASP) with the Heyd-Scuseria Ernzerhof (HSE) hybrid functional. The screening length and the Hartree-Fock mixing parameter are set to 10Å and 0.32, respectively. The valence electron configuration considered are Zn: $3d^{10}4s^2$ and S: $3s^23p^4$, while inner electrons are treated as core states within the projector augmented wave (PAW) method. A plane-wave energy cutoff of 420 eV is used. A 64-atom supercell, consisting of 32 Zn and 32 S atoms, is employed to model intrinsic defects. Brillouin zone sampling is performed using a Gamma-centered $2 \times 2 \times 2$ Monkhorst-Pack k-point mesh. Defect formation energies are determined using: $E_d^f = E_{defect} - E_{pristine} - \sum_i n_i u_i + q E_F$. Where $E_{defect} - E_{pristine}$ represents the energy difference upon introducing a single defect in the structure. The remaining terms account for mass and charge compensation. n_i is the added (positive) or removed (negative) number of atoms of species i with chemical potential u_i . q is the defect charge state, and E_F is the Fermi level.

Supplementary Information

References

1. Migliori A, *et al.* Resonant ultrasound spectroscopic techniques for measurement of the elastic moduli of solids. *Physica B: Condensed Matter* **183**, 1-24 (1993).
2. Migliori A. Resonant ultrasound spectroscopy. Los Alamos National Laboratory (LANL), Los Alamos, NM (United States) (2016).
3. Hutson A, White DL. Elastic wave propagation in piezoelectric semiconductors. *Journal of Applied Physics* **33**, 40-47 (1962).
4. García de Arquer FP, Talapin DV, Klimov VI, Arakawa Y, Bayer M, Sargent EH. Semiconductor quantum dots: Technological progress and future challenges. *Science* **373**, eaaz8541 (2021).
5. Shockley W, Read Jr W. Statistics of the recombinations of holes and electrons. *Physical review* **87**, 835 (1952).
6. Findlay P, *et al.* Auger recombination dynamics of In_xGa_{1-x}Sb. *Semiconductor science and technology* **14**, 1026 (1999).
7. Rose A. Recombination processes in insulators and semiconductors. *Physical Review* **97**, 322 (1955).
8. Meng X, *et al.* Giant superlinear power dependence of photocurrent based on layered Ta₂NiS₅ photodetector. *Advanced Science* **10**, 2300413 (2023).
9. Schubert EF. *Light-emitting diodes*. Cambridge university press (2006).
10. Jones DI. *Handbook of viscoelastic vibration damping*. John Wiley & Sons (2001).
11. Saxena T, Rumyantsev S, Dutta P, Shur M. CdS based novel photo-impedance light sensor. *Semiconductor Science and Technology* **29**, 025002 (2014).
12. Karazhanov SZ, Lew Yan Voon L. Ab initio studies of the band parameters of III–V and II–VI zinc-blende semiconductors. *Semiconductors* **39**, 161-173 (2005).
13. Wei S-H, Zunger A. Calculated natural band offsets of all II–VI and III–V semiconductors: Chemical trends and the role of cation d orbitals. *Applied Physics Letters* **72**, 2011-2013 (1998).
14. Hübner K. Piezoelectricity in Zincblende- and Wurtzite-Type Crystals. *physica status solidi (b)* **57**, 627-634 (1973).
15. Ho QD, Castillo M. Defects study in zinc blende ZnS utilizing optimized hybrid functional.

Supplementary Information

Computational Materials Science **216**, 111827 (2023).

16. Li P, Deng S, Zhang L, Liu G, Yu J. Native point defects in ZnS: First-principles studies based on LDA, LDA+ U and an extrapolation scheme. *Chemical Physics Letters* **531**, 75-79 (2012).
17. Varley J, Lordi V. Electrical properties of point defects in CdS and ZnS. *Applied Physics Letters* **103**, (2013).
18. Seebauer EG, Kratzer MC. Charged point defects in semiconductors. *Materials Science and Engineering: R: Reports* **55**, 57-149 (2006).